atmosphere

MDPI

Article

Coupled Stratospheric Chemistry–Meteorology Data Assimilation. Part I: Physical Background and Coupled Modeling Aspects

Richard Ménard [1,*,†], Simon Chabrillat [2,†], Alain Robichaud [1], Jean de Grandpré [1], Martin Charron [3], Yves Rochon [1], Rebecca Batchelor [4,‡], Alexander Kallaur [1,§], Mateusz Reszka [5] and Jacek W. Kaminski [6]

1 Air Quality Research Division, Environment and Climate Change Canada, 2121 Transcanada Highway, Montréal, QC H9P 1J3, Canada; alain.robichaud@canada.ca (A.R.); jean.degrandpre@canada.ca (J.d.G.); yves.rochon@canada.ca (Y.R.); Alexander.Kallaur@canada.ca (A.K.)
2 Royal Belgian Institute for Space Aeronomy, BIRA-IASB, 1180 Brussels, Belgium; simon.chabrillat@aeronomie.be
3 Meteorological Research Division, Environment and Climate Change Canada, Montréal, QC H9P 1J3, Canada; martin.charron3@canada.ca
4 Department of Physics, University of Toronto, Toronto, ON M5S 1A7, Canada; r.batchelor@gmail.com
5 Data Assimilation and Quality Control Section, Canadian Center for Meteorological and Environmental Prediction, Montréal, QC H9P 1J3, Canada; mateusz.reszka@canada.ca
6 Institute of Geophysics, Polish Academy of Sciences, 01-452 Warsaw, Poland; jkaminski@ecoforecast.net
* Correspondence: richard.menard@canada.ca; Tel.: +1-514-421-4613
† These authors contributed equally to this work.
‡ Current address: PROUD Program, University of Puerto Rico Humacao PR-908, San Juan, PR 00792, USA.
§ Current affiliation: Shared Services Canada, HPC (High Performance Computing) Division, 2121 Transcanada Highway, Montréal, QC H9P 1J3, Canada.

Received: 19 October 2019; Accepted: 21 January 2020; Published: 30 January 2020

Abstract: A coupled stratospheric chemistry–meteorology model was developed by combining the Canadian operational weather prediction model Global Environmental Multiscale (GEM) with a comprehensive stratospheric photochemistry model from the Belgian Assimilation System for Chemical ObsErvations (BASCOE). The coupled model was called GEM-BACH for GEM-Belgian Atmospheric CHemistry. The coupling was made across a chemical interface that preserves time-splitting while being modular, allowing GEM to run with or without chemistry. An evaluation of the coupling was performed by comparing the coupled model, refreshed by meteorological analyses every 6 h, against the standard offline chemical transport model (CTM) approach. Results show that the dynamical meteorological consistency between meteorological analysis times far outweighs the error created by the jump resulting from the meteorological analysis increments at regular time intervals, irrespective of whether a 3D-Var or 4D-Var meteorological analysis is used. Arguments in favor of using the same horizontal resolution for chemistry, meteorology, and meteorological and chemical analysis increments are also presented. GEM-BACH forecasts refreshed by meteorological analyses every 6 h were compared against independent measurements of temperature, long-lived species, ozone and water vapor. The comparison showed a relatively good agreement throughout the stratosphere except for an upper-level warm temperature bias and an ozone deficit of nearly 15%. In particular, the coupled model simulation during an ozone hole event gives better ozone concentrations than a 4D-Var chemical assimilation at a lower resolution.

Keywords: coupled chemistry–meteorology model; dynamical–photochemical–radiation interactions in the stratosphere; comparison between online model and offline CTM approach

1. Introduction

This two-part paper describes and examines the benefits of a coupled meteorology–stratospheric chemistry data assimilation system, using the Canadian Meteorological Center (CMC) Numerical Weather Prediction (NWP) model and a comprehensive stratospheric chemistry model, BASCOE (Belgian Assimilation System for Chemical ObsEvations), both validated in their respective environment (i.e., meteorology/chemistry) with data assimilation capabilities. Assimilation experiments, using both weak and strong data assimilation coupling, are presented in Part II [1]. Here in Part I we cover primarily topics relevant to Part II. We examine; 1—the physical basis of stratospheric chemistry–meteorology interactions, 2—model coupling aspects such as the resolution of each geophysical model component (meteorology, chemistry) and whether it should be offline or online in order to yield the most accurate chemical representation, and 3—an evaluation of the coupled model in the context of data assimilation.

The last item deserves some explanation. In model evaluation we should distinguish between unconstrained climate models and atmospheric models where the stratospheric dynamics is constrained by the assimilation of temperature (i.e., radiances). In climate models we compare the climatology of the model against the climatology of the observations. However, data assimilation is based on using the instantaneous observed values at their specific locations. We know that the atmospheric dynamics is chaotic, and its model representation is very sensitive to initial conditions. Atmospheric chemistry models are quite different in that respect; the chemistry is strongly dependent on the meteorology as well as chemical sources and sinks. A free chemistry simulation, without chemical data assimilation but driven by meteorological analyses, can in fact be compared to a reasonable degree of accuracy, to chemical observations at their proper time and location [2]. Therefore, this is the framework we want to use in our chemical modeling evaluation. Furthermore, data assimilation schemes are based on the assumption that differences between observations and model values at their proper time and location (called innovations) are essentially random rather than systematic. In the case where systematic differences are comparable to or exceed the random error standard deviation, the assimilation system is sub-optimal and observations can have little impact (and can even be detrimental, such as introducing spurious spatial structures).

Traditionally, Chemical Transport Models (CTM's) [3,4] have offered the most complete chemical representation and are often used as benchmarks for chemistry. CTM's are usually driven offline by meteorological analyses. While the meteorological analyses are usually (and practically) only available at 6 or 12 h time intervals, the meteorology has to be interpolated in time in order to give a dynamical field to drive the chemistry at each model time step. Clearly an offline CTM cannot be used to study the impact of the chemistry on the meteorology.

It is interesting to note the complementary nature of Numerical Weather Prediction (NWP) models with CTMs. Indeed, NWP models solve for; (a) momentum, (b) thermodynamics, (c) conservation of mass and aside from water vapor, (d) use climatological fields as input for chemical composition (in particular ozone and greenhouse gases). In contrast, CTMs; (a) provide a comprehensive representation of chemical composition, (b) solve for the conservation of mass of individual species using chemical reactions and photochemistry, (c) but require as input the momentum (winds), thermodynamics (temperature) and total mass (surface pressure). NWP models routinely use data assimilation, and several CTM's also have (chemical) data assimilation capabilities. By bringing together these two approaches we can develop a fully coupled chemistry–meteorology model with data assimilation capabilities.

Coupled meteorology-chemistry models provide not only a consistent treatment of the processes shared by meteorology and chemistry but also allow for three-way interactions between physical, chemical and radiation processes [5]. Coupled meteorology-chemistry models are used in several areas such as; (1) in climate simulations with Global Chemistry Circulation Models (GCCMs) [6–8] and in climate-chemistry process validation [9,10], (2) for air quality modeling and prediction [11,12], (3) to examine the impact of chemical composition on weather prediction [5,13],

and (4) in chemical-meteorology reanalysis such as using weak data assimilation coupling with aerosol-radiation interaction [14,15], or with an ensemble data assimilation but with no interaction and no cross-covariances between species or between species and meteorology [16,17], or using 4D-Var but with chemical increments decoupled from meteorology increments [18]. This wide range of modeling activity is also nicely summarized in a WMO GAW report [19].

The above four classes of coupled models differ somewhat from each other. While GCCM's consider simulations on multi-decadal to century timescales, air quality models and numerical weather prediction models coupled with air quality focus on time scales of hours to a year. Chemical reanalysis models lie somewhere in between, focusing on periods of a year to a decade. Chemistry climate models and GCCM's typically have a lower horizontal and vertical resolution than NWP models and generally have limited chemistry composition modeling aimed primarily at simulating GHG (greenhouse gases), aerosols, and aerosol precursors such as those involved in the sulfur cycle (e.g., [20]). When used in process studies (e.g., [10]) or in comparison with observations, these models are usually forced towards meteorological analyses. This may be accomplished either by replacing the model dynamical fields by meteorological analyses (which we call *meteorological refresh*) or by *specified dynamics* [7] that consist of a linear relaxation technique to force incrementally the dynamical fields towards linearly interpolated (in time) meteorological analyses (usually called *analysis nudging*) [21] (not discussed here; see e.g., Froidevaux et al., 2019 [22] for a comparison between the free-running and Specified-Dynamics (SD) configurations of WACCM). In all these cases, except for the GCCM, the radiation feedback on meteorology cannot be examined.

In contrast, air quality models and NWP models coupled with air quality models (classes 2 and 3 above) focus on shorter timescales, have higher resolution both horizontally and vertically and have comprehensive chemistry and aerosol physics and dynamics. Such coupled models allow for the direct assimilation of meteorological observations but are generally used for tropospheric applications [5]. Although temperature and winds have an important effect on the chemical transport and composition in the stratosphere, ozone has an impact on lower stratosphere temperature predictability [23].

In this study, we have constructed such a coupled model starting from the Canadian operational meteorological model [24] GEM (Global Environmental Multiscale model), extended it with relevant physical processes in the stratosphere, and combined it with a comprehensive stratospheric chemical transport model, BASCOE (where as an offline model it has been validated using four-dimensional variational assimilation and ensemble Kalman filtering methods for chemical data assimilation [25–28]). This coupled model is called GEM-BACH for GEM-Belgian Atmospheric CHemistry model.

The organization of Part I can be summarized as follows. First we present the physics of the coupling between dynamics, radiation and chemical composition in the stratosphere (Section 2). Then, in Section 3, we describe the formulation of the coupled model, what changes were needed, and discuss the modular design of the chemical interface that allows the meteorological model to run with or without chemistry. We then discuss how coupled models and CTM models can be driven by meteorological analyses, discuss their properties and errors, and through a series of experiments we quantify the errors in each formulation. We also discuss the importance of analysis and model resolution on the accuracy of a simulation and contrast it with lower-resolution chemical data assimilation. These considerations suggest that the best approach is to drive a coupled model with meteorological analyses. An evaluation of the modeled stratospheric temperatures and chemical species is then carried out, leading to important considerations for the assimilation component addressed in the second part of this study.

2. Physical Background on Dynamical–Photochemical–Radiation Interactions in the Stratosphere

The material presented in this section is general and describes the diverse interactions from a physical point of view. It applies to both Part I and Part II, and particularly in Part II for both weak and strong data assimilation coupling experiments and the prescription of the error covariances.

From the point of view of energy there are two sources which have a profound impact on the temperature and circulation that characterizes the stratosphere; one is of chemical origin and the other of wave/mechanical origin.

Several tropospheric chemical source species which enter the stratosphere (e.g., O_2, H_2O, N_2O, CFC's) are photo-dissociated by solar ultra-violet light, producing chemically active (fast reacting) species (e.g., O, OH, NO, ClO, ... ; see Table 1 for a more complete list). That is the case for molecular oxygen, which is the second most abundant atmospheric gas. O_2 is photo-dissociated at an altitude of about 50 km, resulting in atomic oxygen and very rapidly recombines with molecular oxygen giving rise to ozone O_3, and O_3 also recombines with atomic oxygen. These "recombination-type" chemical reactions are exothermic and release so much heat that they transform the vertical stratification of the atmosphere into a deep stable layer from the tropopause up to 50 km, which characterizes the stratosphere. These chemical reactions are known collectively as the Chapman mechanism and are identified with (*) in Tables A1 and A3 of Appendix A. The ozone chemistry also involves catalytic loss cycles with the hydrogen (HOx), nitrogen (NOx), and halogen (ClOx, BrOx) families, which generate other constituents and in particular stable (long-lived) molecules called *reservoir species* (e.g., [29]).

Figure 1 is a diagram of the dynamical-photochemical-radiative interactions in the stratosphere. This major source of heating which is associated with the production of ozone is depicted as a pink arrow in the figure (lower left side). On a global, yearly averaged scale, the heating is nearly counterbalanced by infrared cooling by CO_2, and by O_3 (about half of the effect of CO_2), with a small contribution due to H_2O [30] (see Figure S1 in Supplementary Material).

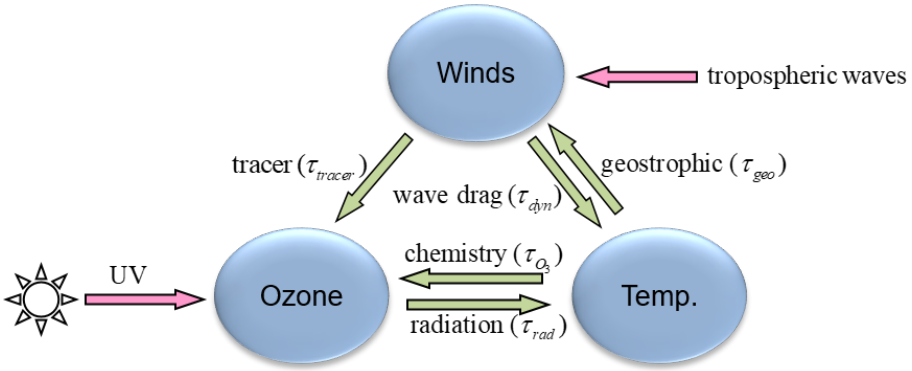

Figure 1. Dynamical–photochemical–radiation interactions in the stratosphere.

The other important source of energy in the stratosphere is mechanically driven by the drag force due to breaking waves of tropospheric origin. In contrast to the troposphere, where diabatic heating creates vertical motion, it is the mechanically driven circulation in the stratosphere which induces vertical motion of which diabatic heating (in isentropic coordinates) is an outcome and not a cause [31,32]. This source of energy is depicted as the second pink arrow in Figure 1 (upper right side).

The wave drag is explained by the breaking of vertically propagating Rossby and gravity waves in the stratosphere [31]. Planetary-scale Rossby waves, which are forced by orography and land-sea contrasts, can propagate upward only in westerly flow and can reach the stratosphere. Depending on the background mean zonal wind and the wavelength, Rossby waves can become stationary and have growing amplitudes. If, in addition, there is shear flow, tongues of potential vorticity [33–36] develop, and show up in chemical tracer fields as filamentary structures with cutoff features when the Rossby wave is breaking (e.g., as shown with chemical data assimilation [37]). When the waves break, which occurs at the limit of the diffusion length-scale, they transfer their westward momentum to the zonal flow, thus decelerating it—the so-called wave drag.

Gravity waves have the property that their amplitude increases with height as a result of the decreasing air density. Gravity waves excited by orography reach their critical (breaking) level in

the upper troposphere and lower stratosphere [38], whereas those induced by non-stationary waves (such as in frontal systems) break at higher altitudes and play a major role in the middle-atmosphere general circulation [39,40]. The horizontal scale of these gravity waves are much smaller than the typical resolution of global models and thus both their generation and impact must be parameterized.

The wave drag induces a meridional circulation which changes temperatures in isentropic coordinates. Since angular momentum is conserved, the zonal momentum balances the wave drag, and thus implies a negative mechanical forcing that needs to be compensated by a poleward meridional mass flux due to the Coriolis effect. By mass conservation, the meridional mass flux is also linked to the vertical mass flux, creating a meridional circulation with ascent near the tropics and descent near the poles. This is the Brewer–Dobson circulation [31,32,41,42] (see white arrow Figure S2 in Supplementary Material). The vertical motion across isentropes might seem at first perplexing, but a slow persistent vertical motion can move air parcels across isentropes due to the relaxation effect of radiation. Indeed, if an air parcel is displaced downward at a given location, the immediate response is to warm it adiabatically. Then, as the temperature locally rises above the radiative equilibrium temperature, it experiences infrared cooling, which allows the downward displacement to continue. In an isentropic vertical coordinate system (i.e., in a coordinate based on potential temperature) the vertical velocity simply equals the net diabatic heating. The stratospheric meridional circulation that is driven by forces of tropospheric origin pulls the middle atmosphere away from the radiative equilibrium locally, but not globally on long time scales.

2.1. Ozone-Temperature Interaction

Ozone and temperature are related through radiation and photochemistry, but each process results in different ozone-temperature correlations and has its own timescales (see right and left horizontal green arrows in Figure 1). We will discuss first the processes and then their timescales.

The absorption of solar UV radiation in the production of ozone creates a rapid, local increase in temperature, which pulls the temperature away from radiative equilibrium. The perturbed air parcel then undergoes infrared cooling on a slower timescale, τ_{rad}, and an adjustment towards a new but higher equilibrium temperature value takes place. Thus, there is a positive correlation between O_3 and temperature because of radiative coupling.

The photochemistry gives a different correlation. Since chemical reaction rates depend on temperature, the ozone production rate increases with decreasing temperature. In terms of absolute value, correlations as high as 0.9 have been reported, based on ozone and temperature measurements from MLS [43] and CRISTA [44]. Several authors have pointed out [43,45–47] that the temperature dependence can be represented by a function of the form,

$$O_3 = B \exp\left(\frac{\Theta}{T}\right) \tag{1}$$

where B and Θ are constants whose values depend on the reactants involved in the photochemistry. Taking the derivative of Equation (1) we get the perturbation equation,

$$\frac{\Delta O_3}{O_3} = -\frac{\Theta}{T^2}\Delta T \tag{2}$$

which shows that temperature perturbations give rise to negatively correlated ozone perturbations.

Let us now discuss the timescales of the different processes. To estimate the radiative timescale τ_{rad} we can use the Newtonian cooling approximation to compute the time required to cool an air parcel through IR emission out to space. This approximation is generally valid above ~25 km (or 25 hPa) where the radiation exchange between layers can be neglected. For small temperature perturbations, this Cool-to-Space process Q^{CtS} can be written as $Q^{CtS} = -\alpha(T - T_{rad})$ where T_{rad} is a reference temperature near radiative equilibrium and $\tau_{rad} = 1/\alpha$ is the radiative relaxation timescale. This parameter has been estimated with the GEM-BACH model using a centered finite

difference expression $\tau_{rad} = 2\delta T/[Q(T+\delta T) - Q(T-\delta T)]$ [48] and is displayed in the panel (a) of Figure 2 as a function of latitude and height for a given summer day. Please note that the lower the temperature, the longer is the radiative timescale, thus τ_{rad} decreases with altitude so that a rapid adjustment of the temperature perturbations by the Cool-to-Space process occurs. In the lower stratosphere below (below ∼20 hPa), the radiative timescale is on the order of one month or more, indicating that the temperature perturbations can accumulate over that time period and consequently produce a significant temperature response. The lower stratosphere is thus sensitive to ozone–radiation perturbations.

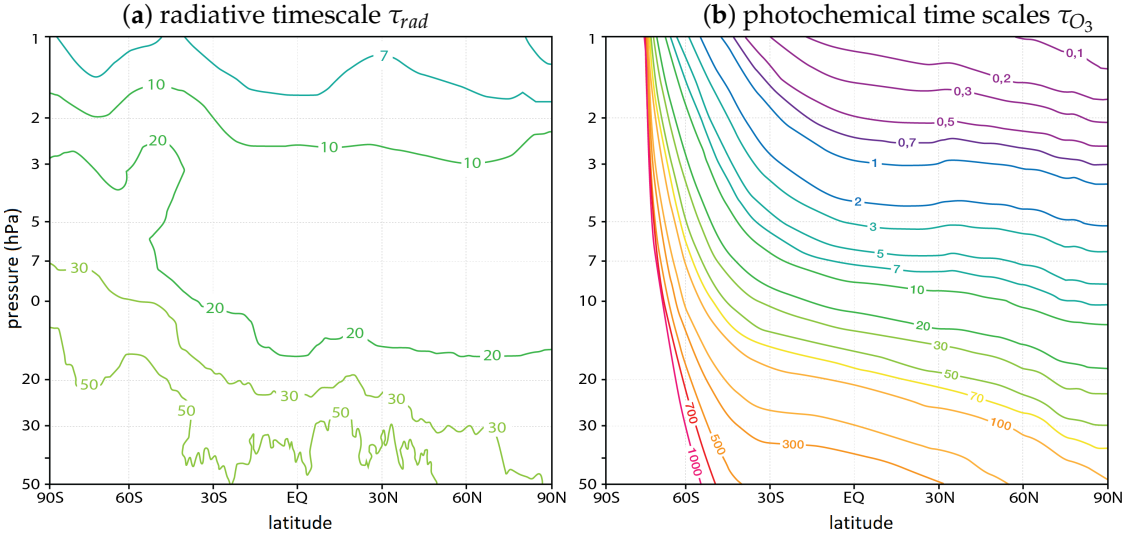

Figure 2. Ozone radiative (**a**) and photochemical time scales (**b**) in days. June first conditions. Please note that south of ∼70° S is the polar night.

The ozone photochemical lifetime τ_{O_3} can be defined as the time required for ozone to be reduced by a factor $1/e$ through photochemical reactions. This timescale is readily available from linearized ozone chemistry schemes such as the LINOZ model [49], $dO_3/dt = c_1 + c_2(O_3 - \overline{O_3}) + c_3(T - \overline{T}) + c_4(O_3^{\uparrow} - \overline{O_3^{\uparrow}})$ which represents the tendency of daily mean values. The overbar denotes the climatology, the $\uparrow$ denotes the overhead column of ozone, and the coefficients c_1, c_2, c_3, c_4 are determined using a chemical box model. The photochemical timescale for ozone is then $\tau_{O_3} = 1/c_2$, which is plotted in panel (b) of Figure 2 for 1 June conditions. Please note that the region south of 60° S is in polar night, and the photochemical timescale is infinite.

Comparing the photochemical timescale τ_{O_3} with the radiative timescale τ_{rad} in sunlight conditions we note that above ∼10 hPa, $\tau_{O_3} << \tau_{rad}$. The ozone–radiation feedback is small because the lifetime of ozone perturbations is too short to have a significant radiative effect. This is the *photochemistry-dominated region*, in which ozone and temperature perturbations are negatively correlated. In this region the assumptions for chemical transport modeling are valid, as there is no need to change the temperatures. Below ∼10 hPa, we have $\tau_{O_3} >> \tau_{rad}$ and the ozone behaves as a passive tracer since the photochemistry can be neglected, but the radiative forcing associated with ozone perturbations persists over several weeks. The ozone radiative impact on temperature can be significant even though the radiative forcing itself is small. Thus, below ∼10 hPa is the *radiation-dominated region* where ozone and temperature perturbations are positively correlated and there are benefits from a coupled radiation-chemistry model approach.

2.2. Temperature-Wind Interaction

Horizontally, most of the stratosphere is in geostrophic balance, except between about 20° N and 20° S and the upper-stratosphere and mesosphere due to gravity wave breaking. For example,

the geostrophic winds derived from satellite observations provided by the CRISTA instrument showed that on a day-to-day basis these winds are remarkably close to the stratospheric winds in the UKMO meteorological analysis [50]. From a dynamical perspective, local perturbations of the horizontal wind and temperature adjust to a balanced state on short time scales (typically less than six hours) by dispersing away fast-moving inertia-gravity waves—a process known as geostrophic adjustment. A scale analysis using the shallow water model reveals that the Rossby number, defined as $R_o = U/fL$, determines the type of adjustment that will take place: when $R_o < 1$, the temperature tends to adjust to the wind field, and when $R_o > 1$, the wind field tends to adjust to the temperature field (f is the Coriolis parameter and L the length-scale of the disturbance). For planetary-scale waves, such as vertically propagating Rossby waves that enter the stratosphere, $R_o < 1$ so that the wind field adjusts to the temperature field. On the other hand, gravity waves of tropospheric origin generally have $R_o > 1$, so that the temperature is adjusted to the wind field. Because this adjustment process is mostly completed after six hours, the short term forecast error used in an intermittent assimilation cycle, are in geostrophic balance. In geostropic balanced flow the vertical rate of change of the wind is related to the horizontal temperature gradient by the so-called *thermal–wind relation*,

$$\frac{\partial u}{\partial p} = \frac{R}{fp}\left(\frac{\partial T}{\partial y}\right)_p \quad ; \quad \frac{\partial v}{\partial p} = -\frac{R}{fp}\left(\frac{\partial T}{\partial x}\right)_p, \tag{3}$$

where u and v are the zonal and meridional wind components, p is the pressure, R the gas constant, and T the temperature. The thermal–wind relation introduces a three-dimensional coupling between temperature and winds, and the timescale associated with this coupling is on the order of the geostrophic adjustment timescale, τ_{geos} (depicted as the slanted leftward green arrow in Figure 1).

On a much longer timescale and as a result of the Brewer–Dobson circulation, the vertical wind and temperature are also related, but as explained earlier (beginning of Section 2), it is the vertical motion, induced by wave breaking, that determines the temperature distribution. Since the radiation relaxation takes place on a timescale which is faster than the residual circulation, the temperature adapts to a new radiative equilibrium as the fluid particles rise in the tropics or descend in the polar regions. On this slow timescale, we thus observe that the vertical motion drives the temperature change and not the reverse. The timescale τ_{dyn} appearing in Figure 1 refers to the slow timescale associated with the residual circulation.

2.3. Wind-Tracer Interaction

Winds drive the transport of chemical species. From a physical point of view, the chemical tracer mixing ratios have no impact on the winds. For ozone there could be an indirect impact through the radiation followed by geostrophic adjustment, but it is known to be a small, second-order effect, considered to be negligible [51,52].

It has also been observed from aircraft, balloon and satellite platforms that long-lived species display compact relationships in concentrations between species. Also, species with very different sources and sinks exhibit nearly identical meridional-vertical isopleth shapes, indicating that it is the atmospheric transport which maintains these relationships. It was argued [53] that if the sources and sinks are sufficiently slow compared with dynamical timescales, then the meridional slopes of mixing ratio isopleth and the compact correlations between different species are determined by quasi-horizontal mixing. Indeed, the tendency to flatten the isopleths that results from quasi-horizontal mixing is larger than the mean overturning circulation (i.e., the Brewer–Dobson circulation), which tends to steepen the isopleths [53,54]. Depending on the process being considered, the timescales of the tracer-wind relationship occur on a wide range of values; from $U/\Delta x$ if no mixing is considered, to timescale longer than a few weeks, but smaller than the Brewer–Dobson circulation timescale.

3. Description of the Coupled Meteorology-Chemistry Model

An online stratospheric chemistry–meteorology model was developed by combining the Canadian GEM (Global Environmental Multiscale) NWP model with the Belgian stratospheric offline chemical transport model (CTM) [24–26,55,56]. The NWP model version used in this study with a lid at 0.1 hPa, has been described and validated by Charron et al. [57] using a variational assimilation system for the assimilation of weather variables [55,56]. This model version became operational for NWP in 2009, but relied on a climatology of stratospheric ozone and did not include any representation of stratospheric chemistry (except for a simple parameterization of water vapor).

The Belgian CTM had a comprehensive stratospheric chemistry and had been delivering operational 4D-Var chemical analyses and forecasts for several years prior to the start of this study. The Belgian operational chemical analysis and forecast system is known as BASCOE and the resulting coupled model was named GEM-BACH (GEM with the Belgian Atmospheric CHemistry). The reader should note, however, that in the years our study took place, only a tropospheric version of GEM (with top at 10 hPa) was operational, so we conducted, ourselves, the tropospheric-stratospheric meteorological assimilation using AMSU-A channels 11–14 for the stratosphere.

Both modeling systems had the necessary components to produce a realistic representation of the stratosphere. The chemistry of the BASCOE CTM, which used a flux-form semi-Lagrangian method for transport [58] was extracted and implemented through a chemical interface in GEM. The resulting chemical transport was then a semi-Lagrangian advection. The stratospheric chemistry component (discussed in Sections 3.2 and 3.3) and the chemical interface (described in Section 3.4) made the final model fully integrated, from both a dynamical and ozone–radiation interaction perspective, as well as modular (e.g., allowing switching between different chemical packages or running without chemistry).

3.1. Meteorological Model

GEM is a two time-level semi-Lagrangian fully implicit non-hydrostatic grid point model [24] which uses either uniform or variable horizontal-resolution grids [59]. An Arakawa C discretization is used in the horizontal and a hybrid vertical coordinate with non-staggered finite differences is used in the vertical. The model solves for horizontal and vertical momentum, thermodynamics, continuity, and the advection of an arbitrary number of tracers. For the stratosphere, additional physical parameterizations were added including a non-orographic gravity wave drag (GWD) [39,40] scheme for representing the breaking of unresolved non-stationary waves which has a major impact on the middle-atmosphere general circulation. For the computation of radiative transfer the model uses a radiation scheme based on the k-correlated distribution method [60] which is an efficient approach to compute the radiation using a limited number of absorption coefficients. The radiation scheme also uses an ozone climatology based on Fortuin and Kelder (1998) [61] which is merged with HALOE observations above 0.5 hPa. Finally, a stratospheric water vapor parameterized is employed, via a simple methane oxidation mechanism [62,63]. The description and validation of the stratospheric extension of GEM is discussed in Charron et al. (2012) [57].

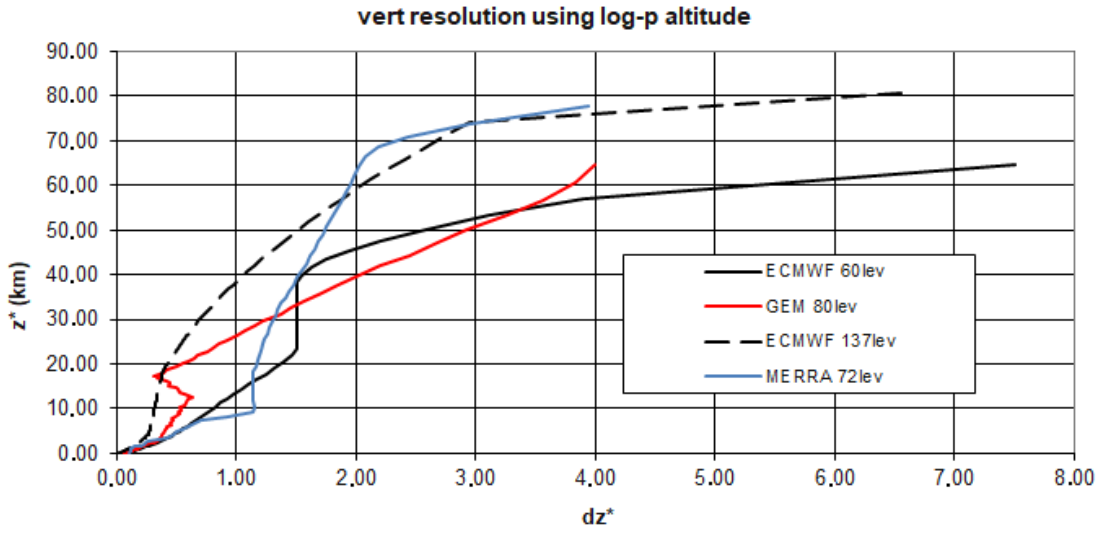

Figure 3. Approximate distributions of the vertical levels of four typical assimilation systems whose domains include the full stratosphere: the ECMWF vertical grid with 60 levels, used for ERA-Interim (black solid line); the ECMWF grid with 137 levels, used operationally and for ERA-5 (black dashed line); the GMAO grid with 72 levels, used for MERRA (blue line) and the GEM or GEM-BACH grid extended to 80 levels which is used here (red line).

GEM-BACH used here is configured to run in hydrostatic mode with a global uniform resolution of 1.5° × 1.5°, i.e., 240 × 120 grid points. The vertical domain extends to 0.1 hPa and uses 80 vertical levels, 27 of which are in the stratosphere. Such high vertical resolution is uncommon to most Global Chemistry Climate Models (GCCM's) which is a distinctive feature of the coupled model GEM-BACH. Figure 3 compares the vertical grid used in this study with the ECMWF vertical grid used back in 2005 (at the beginning of this study). Altitude and vertical grid spacing are estimated using log-pressure altitudes ($z^* = H \ln(p_0/p)$), where the surface pressure p_0 is set to 1000 hPa and the scale height H is set to 7 km.

A series of meteorology-only climate simulations at a resolution of 1.5° × 1.5° using the additional stratospheric parameterizations (outlined above) was performed and the results were compared against either ERA 40 climatology or observations (see Figures S3–S5 in the Supplementary Material). We observed that the native run (a version of the model with a top at 0.1 hPa but with no stratospheric physical parameterizations), exhibit a tropical tropopause and polar winter stratosphere which were too cold while the summer pole stratosphere was too close to radiative equilibrium. But with these stratospheric parameterizations these issues were significantly corrected compared with the ERA 40 reanalysis. Corrections to the zonal winds were also observed with these additional parameterizations (Figure S4 Supplementary Material), where the Hines GWD scheme reduced the mesospheric jets and the new radiation scheme intensified the zonal wind in the stratosphere. The representation of interannual variability in the zonal winds, obtained from a zonal wind time series in the tropics, was also reasonably well captured with these additional parameterizations (Figure S5 in Supplementary Material).

3.2. Stratospheric Chemistry Model

The photochemical module that has been implemented in GEM-BACH is the one used by the Belgian Institute for Space Aeronomy (BIRA-IASB) which includes 57 species, interacting through 143 gas-phase reactions, 48 photolysis reactions and 9 heterogeneous reactions. Table 1 gives the list of species and Appendix A details the list of photochemical reactions. Appendix B explains the physics of the photochemical reaction rates, the so-called J values. Appendix C gives the lower chemical boundary condition at 400 hPa, the level blow which the chemistry solver is not active. The chemical

reaction rates and photodissociation rates follow the Jet Propulsion Laboratory compilation [64]. A complete description of the stratospheric chemistry is not intended to be covered here, and we refer the interested reader to appropriate review papers (e.g., [29]).

Table 1. List of chemical species in BASCOE.

Source species	
Natural	$H_2O, N_2O, CH_4, CH_3Cl, CH_3Br$
Anthropogenic	CFC-11 ($CFCl_3$), CFC-12 (CF_2Cl_2), CFC-113, CFC-114, CFC-115, HA-1301 ($CBrF_3$), H-1211 ($CBrClF_2$), HCFC-22 ($CHClF_2$), $CCl_4, CH_3CCl_3, CHClF_2, CHBr_3$
Short-lived species	
Oxygen (O_x)	$O_3, O(^1D), O(^3P)$
Hydrogen (HO_x)	H, OH, HO_2, H_2O_2
Nitrogen (NO_x)	N, NO, NO_2, NO_3
Chlorine (ClO_x)	$ClOO, OClO, Cl, ClO, ClNO_2, HOCl, Cl_2O_2, Cl_2$
Bromine (BrO_x)	$Br, Br_2, BrO, BrCl, HOBr$
Hydrocarbons (HC)	$CH_3, CH_3O, CH_3O_2, CH_2O, CH_3OOH$
Long-lived species	
	$HNO_3, HNO_4, N_2O_5, ClONO_2, BrONO_2$
	$HBr, HCl, CO, HF, HCO, H_2$

The rates for gas-phase and heterogeneous chemistry depend on temperature. A reaction between two molecules has a reaction rate k_g of the form

$$k_g = Ae^{E/RT}, \tag{4}$$

where E represents the energy of activation, R is the gas constant and A the Arrhenius factor. Reactions involving three molecules can also be pressure-dependent and require more complex formulations. Reaction rates involving aerosols are generally expressed as

$$k_{ae} = \frac{\gamma}{4}\left(\frac{8kT}{\pi M}\right)^{1/2} A_{ae} \tag{5}$$

where the term in parentheses represents the molecular mean speed of the gas-phase molecules, which depends on temperature T, the molecular mass M, and the Boltzman constant k. A_{ae} is the aerosol surface area per unit volume and γ is the reaction efficiency representing the probability that a reaction takes place following the collision of the molecule with the particle. Chemical rate coefficients are determined experimentally and tabulated for different conditions [64].

Heterogeneous chemistry plays an important role, especially in polar regions, and has been explicitly taken into account in GEM-BACH (see Table A2). Hydrolysis reactions on the surface of Stratospheric Sulfate Aerosols (SSA) contribute mainly to the removal of active nitrogen in the lower stratosphere. In polar regions, another important class of aerosols is Polar Stratospheric Clouds (PSC). Such clouds usually form from SSA particles and grow at cold temperatures from the uptake of water vapor and nitric acid (see [65] for a review). In GEM-BACH, the surface area available for heterogeneous reactions is parameterized in a crude manner. Instead of using a costly detailed microphysical calculation, we used a climatology of SSA surface area densities (see Figure S6 in Supplementary Material). Type II PSC particles (primarily composed of water ice) are set to appear at temperatures below 186°K with a surface area density equal to 5×10^{-9} cm^2/cm^3. Between 186°K and 194°K, they are replaced by Type Ia PSC particles (primarily composed of Nitric Acid Trihydrate, NAT) with the same surface area density. The parameterization of PSCs also incorporates the impact of PSC sedimentation on water vapor (dehydration) and gaseous HNO_3 (denitrification). Exponential

loss is prescribed for these two species, with characteristic times of 9 days for water vapor (at the gridpoints where type II PSCs are present) and 100 days for nitric acid (at gridpoints where type Ia PSCs are present).

Since the onset of heterogeneous chemistry on PSC depends on temperature, it is important that the meteorological model can reach the threshold temperature required. Figure 4 shows the 15-year average temperature over the South Pole region (defined as the area south of 60° S) as function of height and the day of the year. Of course some years are different from others, and the temperature is not completely uniform in the polar vortex, but Figure 4 does indicate that the GEM model reaches temperatures below 190 °C.

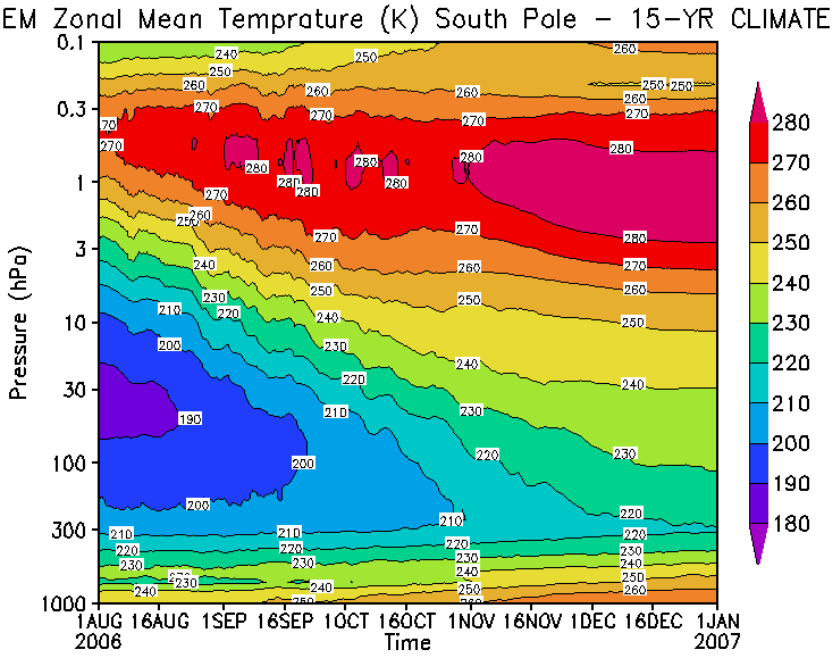

Figure 4. Time series of daily average GEM temperature (over 15 years) over the polar vortex.

3.3. Chemical Solver

The photochemical module and solver used here follow closely those of [66] used at the Belgian Institute for Space Aeronomy (BIRA-IASB). The chemical solver acts on number densities (expressed as molecules-m^{-3}), not on mixing ratios as in transport. Ignoring the issue of advection for the moment, the chemical tendency on a model grid is of the form,

$$\frac{\partial c_i}{\partial t} = P_i(\mathbf{c}) - L_i(\mathbf{c})c_i = \Phi_i(\mathbf{c}), \tag{6}$$

where $\mathbf{c} = (c_1, c_2, ..., c_J)$ is the vector of number densities for J chemical species, $P(\mathbf{c})$ is the production term and $L(\mathbf{c})$ is the loss term. Together they define, $\Phi_i(\mathbf{c})$, the chemical transformation operator for species i. Equation (6) is obtained by adding all the product and loss processes for each species ($i = 1, \ldots, J$) from the list of chemical reactions given in Appendix A. This results in J chemical tendency equations, fewer than the total number of chemical reactions N, ($J < N$). An example of such a procedure is given in Tables 1 and 2 of Yudin and Khattatov (2010) [67]. The photochemical transformation Equation (6) actually forms a set of stiff non-linear equations that span a wide range of chemical timescales. In principle this is best integrated with an implicit time-discretization scheme (e.g., Backward Euler scheme),

$$\mathbf{c}^{n+1} = \mathbf{c}^n + \Delta t \mathbf{\Phi}(\mathbf{c}^{n+1}) \tag{7}$$

which ensures computational stability. However, to deal with the non-linearity of $\mathbf{\Phi}$, a linearization around the state at time t_n (up to second order) can be made,

$$\mathbf{c}^{n+1} = \mathbf{c}^n + \Delta t(\mathbf{\Phi}(\mathbf{c}^n) + \mathbf{J}(\mathbf{c}^{n+1} - \mathbf{c}^n)), \tag{8}$$

where $\mathbf{J} = \partial\Phi/\partial\mathbf{c}$ is the Jacobian of the chemical production and loss terms, leading to a semi-implicit scheme of the form,

$$\mathbf{c}^{n+1} = \mathbf{c}^n + (\mathbf{I} - \Delta t\mathbf{J})^{-1}\Delta t\mathbf{\Phi}(\mathbf{c}^n), \tag{9}$$

which, although it is not guaranteed to be stable, is usually stable in practice. The resulting equation is then linear. The actual numerical scheme that solves the chemistry is a Rosenbrock solver of third-order that is a variant and generalization of Equation (9), where the time step is subdivided into several internal time steps h (here 3) (see [68], [69] Section 16.6, [70]). This solver is made numerically stable through the specification of the coefficient of the Rosenbrock scheme [71]. The Fortran code needed to apply the Rosenbrock solver for the chemical kinetic equations can be built by the Kinetic PreProcessor (KPP) [72] that also determines the appropriate magnitude of h based on a tolerance factor set as 0.1 in the current version of the model. The chemical solver is applied from the model lid to 400 hPa due to the lack of tropospheric chemistry in the model. In the three bottom layers, species mixing ratios are specified to a set of values taken from the SLIMCAT CTM [4] and are shown in Table A4 in Appendix C. Species vertical fluxes are null at the model lid.

The execution of the chemistry solver with a semi-Lagrangian transport scheme proceeds as follows. First, a semi-Lagrangian advection is performed on all species by interpolating from the upstream (i.e., departure) points to compute the mixing ratio at the arrival point on the model grid. Please note that all species have the same upstream point and interpolation weights, which are calculated only once. This represents a significant computational savings for the chemical transport. The species mixing ratio is converted into number density and the photochemical tendency for each species is computed on each model grid point. Once the number densities are updated, they are transformed back into mixing ratios for another transport time step or for a call to the physics scheme. The transformation from number density to mixing ratio follows the expression $\chi = (R_* T / N_A\, p)\, c$, where T is the temperature, p the pressure, R_* the universal gas constant, and N_A the Avogadro number.

3.4. Model Coupling and Interface

Models are composed of several processes which are integrated either sequentially or in parallel (simultaneously). In sequential processing, for a given time step, the model state is updated after each process and provides input to the next process, until all processes are integrated. Sequential processing is also called time-splitting. In parallel processing, the tendencies of each process are computed simultaneously using the same initial model state. The updated state is computed from the sum of tendencies. Parallel processing is also called process splitting.

Parallel processing is appealing because of its simplicity and ease of implementation for coupled models. However, it has the disadvantage that the stationary solution of the time-discrete equation does not match the stationary solution of the time-continuous equation [73,74]. Sequential processing does not have this problem—it has the same stationary solution as the time-continuous equation. However, the transient solution depends on the order in which the different processes are integrated. The total error is minimized when the processes are ordered from the slowest process to the fastest [75,76].

The meteorological model GEM uses sequential processing and we have followed closely the same approach for the coupled meteorology-chemistry model configuration. In addition, we have adopted a modular design such that the chemistry component can be present (or not) through a chemical interface. This flexibility allows having a meteorology-only or meteorology-chemistry model configuration. However, this flexibility entails a small additional computational cost and maintenance, since some physics routines need to be duplicated and present in the chemical module. To make

this clear let us begin by discussing what sequential processing would look like if chemistry were completely integrated with the physics module.

The processes in the meteorological model GEM are updated in the following sequence: 1—Radiation, 2—Advection, 3—Dynamics terms of meteorological variables using a semi-implicit scheme, 4—Surface fluxes and gravity wave drag (orographic and non-orographic), 5—Boundary layer processes and vertical diffusion, 6—Shallow convection, 7—Deep convection, and 8—Microphysics. A coupled meteorology-chemistry model has a 9th process—Chemistry, which involves very fast process that in principle should be solved implicitly but in practice we have chosen to use a semi-implicit approach using a Rosenbrock solver (see Section 3.3). For the purpose of this discussion let us consider only those processes that involve both meteorological and chemical variables. For stratospheric chemistry those are: 1—Radiation, 2- Advection, 5—Vertical diffusion, and 9—Chemistry.

Let $\mathbf{X}$ represent the coupled (augmented) state vector, i.e.,

$$\mathbf{X} = \begin{pmatrix} \mu \\ \chi \end{pmatrix} \tag{10}$$

where μ is the meteorological state vector and χ the chemical state vector. Then the evolution that matters for the coupled state vector takes the form

$$\frac{D\mathbf{X}}{Dt} = \mathbf{R}(\mathbf{X}) + \mathbf{D}(\mathbf{X}) + \mathbf{\Phi}(\mathbf{X}) \tag{11}$$

where $D\mathbf{X}/Dt$ represents the material derivative, $\mathbf{R}$ the radiation, $\mathbf{D}$ the vertical diffusion and $\mathbf{\Phi}$ chemical processes.

The radiation $\mathbf{R}(\mathbf{X})$ can be either offline or online with the prognostic chemical variables–in particular O_3. In the offline mode, greenhouse gases and a zonal-mean climatology of O_3 are given as input to the radiation. Our ozone climatology is based on Fortuin and Kelder [61] and HALOE observations above 1 mb. Thus, the radiation process takes the form

$$\mathbf{R}(\mathbf{X}) = \begin{pmatrix} \mathbf{R}(\mu^n, \overline{\chi^c}) \\ \mathbf{0} \end{pmatrix}. \tag{12}$$

Since radiation in the troposphere depends on cloud parameters that are diagnostic, and thus not advected, and also depends on temperature that is advected, it is desirable to compute radiation before advection in order to avoid any mismatch in the fields required as input. The radiation update thus operates on the initial state $\mathbf{X}^n$ to create an intermediate state $\mathbf{X}^*_R$ of the form

$$\mathbf{X}^*_R = \begin{pmatrix} \mu^*_R \\ \chi^*_R \end{pmatrix} = \mathbf{X}^n + \Delta t \mathbf{R}(\mathbf{X}^n) = \begin{pmatrix} \mu^n + \Delta t \mathbf{R}(\mu^n, \overline{\chi^c}) \\ \chi^n \end{pmatrix} \tag{13}$$

In a fully coupled ozone–radiation configuration that we will consider in Part II of this study [1], the radiation process then takes the form $\mathbf{R} = \mathbf{R}(\mu^n, \chi^n_{O_3})$.

After radiation, advection is processed on both meteorological and chemical variables using $\mathbf{X}^*_R$ as the initial state. Without loss of generality, in a semi-Lagrangian scheme we can write the advection update as,

$$\mathbf{X}^*_A = \begin{pmatrix} \mu^*_A \\ \chi^*_A \end{pmatrix} = \begin{pmatrix} \mu^*_R(\mathbf{x} - \boldsymbol{\alpha}\Delta t) \\ \chi^*_R(\mathbf{x} - \boldsymbol{\alpha}\Delta t) \end{pmatrix}, \tag{14}$$

where $\mathbf{x}$ is the spatial coordinate and $\boldsymbol{\alpha}$ the upstream displacement along the trajectory. The next process to consider is the vertical diffusion $\mathbf{D}(\mathbf{X})$ that is applied on both meteorological and chemical state variables. The resulting update has the form

$$\mathbf{X}_D^* = \begin{pmatrix} \boldsymbol{\mu}_D^* \\ \boldsymbol{\chi}_D^* \end{pmatrix} = \begin{pmatrix} \boldsymbol{\mu}_A^* + \Delta t \mathbf{D}_K(\boldsymbol{\mu}_A^*) \\ \boldsymbol{\chi}_A^* + \Delta t \mathbf{D}_K(\boldsymbol{\chi}_A^*) \end{pmatrix}, \tag{15}$$

using diffusion coefficients K computed from meteorological fields that are common to both meteorological and chemical variables. Finally, the coupled state is updated for the chemical processes,

$$\mathbf{X}^{n+1} = \mathbf{X}_\Phi^* = \begin{pmatrix} \boldsymbol{\mu}_\Phi^* \\ \boldsymbol{\chi}_\Phi^* \end{pmatrix} = \begin{pmatrix} \boldsymbol{\mu}_D^* \\ \boldsymbol{\chi}_D^* + (\mathbf{I} - \Delta t \widetilde{\mathbf{J}}_\mu)^{-1} \Delta t \widetilde{\boldsymbol{\Phi}}_\mu(\boldsymbol{\chi}_D^*) \end{pmatrix}, \tag{16}$$

with a resulting state $\mathbf{X}^{n+1}$. Here in Equation (16), the dependence on μ is actually (T, p), temperature and pressure. We also use the tilde $\widetilde{(\,)}$ to emphasize that the Jacobian and chemistry production and loss terms are evaluated in terms of mixing ratio and not in terms of the number density as in Equation (9).

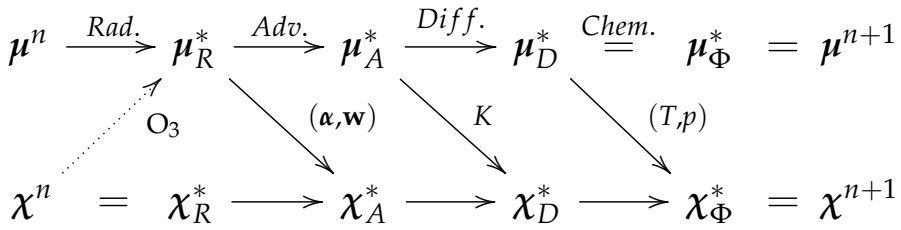

Figure 5. Sequence of processes in the coupled model. Horizontal arrows represent the different process updates as in Equations (13)–(16). The slanted solid arrows represents the exchange of information from meteorological derived fields to the chemistry and the slanted dot arrow from chemistry to meteorology in ozone–radiation coupling.

Figure 5 displays the sequence of updates of the coupled (augmented) model state and which information is passed from meteorological to chemical modules (up and down arrows). The equal sign indicates that there are no changes and the horizontal arrows indicate changes due to a specific process update. To simplify, let us first discuss the case where there is no ozone–radiation coupling, i.e., let us ignore for now the dotted upward arrow.

First, infrared radiation does not change the chemical concentrations but does change the temperature. Then, the advection of chemical (prognostic) variables requires information about the displacement of the upstream point, $\boldsymbol{\alpha}$, and the interpolation weights, $\mathbf{w}$, that are computed from the wind and the position of the upstream point. Next, applying the vertical diffusion on chemical variables requires sharing the diffusion coefficients, K, that are computed from the meteorology. Finally, chemistry requires information about temperature and pressure, but does not change the meteorological variables. When this last update is completed, the state at time t^{n+1} is produced.

In a modular implementation, all processes that involve changes in chemical concentrations (in practice, with the exception of advection) can be included in a chemical module. The computation of the changes in chemical concentrations requires exchange of information through a chemical interface. For example, if we duplicate and include the vertical diffusion routine in the chemical module and pass the K coefficients to the chemistry module, the computation of the vertical diffusion of the chemical variables can be done in the chemistry module. Likewise, in principle, the advection of the chemical variables could be performed in the chemistry module if we duplicate the appropriate routines, but in practice it is easier (in terms of code maintenance), to simply pass the chemical

concentrations to the advection routine that computes advection to all meteorological and chemical variables at once.

So far, the exchange of information is performed only one way, from meteorology to chemistry. It is then possible and easy to have a meteorology-only configuration separate from a meteorology-chemistry configuration, by simply allowing advection to be performed on an arbitrary number of variables.

The modularity of this approach can be preserved with sequential processing in the case of ozone–radiation interaction. Indeed, after the whole sequence of processes from advection to increasingly faster processes is completed, the prognostic ozone can be passed as the initial condition to the radiation scheme for the next model time step integration (see dotted upward arrow in Figure 5).

Finally, in terms of computational resources, GEM-BACH is about five times slower than GEM (with no chemistry) on a uniform resolution $1.5^\circ \times 1.5^\circ$, i.e., 240×120 grid points, with 80 vertical levels, and running on 16 CPU (MPI 4 nodes, OpenMP 4 CPU). GEM-BACH transport (advection of 57 species) accounts for about 1/4 of the CPU time, the computation of the *J*-values for about 1/4 of the CPU time, and the Rosenbrock chemical solver about 1/2 of the CPU time.

4. Coupling with Meteorological Analyses

In data assimilation we pay a lot of attention to errors in the model and the observations. In a coupled model, it may be important to examine the coupling strategy and the resolution of the different model components, in order to minimize the size and/or number of errors. In the next three sections we will examine different source of errors in dynamical model coupling with meteorological analyses and will assess their impact. This will guide us in choosing the way forward for the comparison of the chemistry simulations with observations (Section 7) and to conduct the combined chemical and meteorological assimilation in Part II [1].

By way of introduction of the relevant topics, let us examine the time continuity. The use of (time) sequential meteorological analyses, such as in 3D-Var, creates a temporal discontinuity in the meteorological fields. The question arises then as to "What is the implication for the chemical transported fields".

Depending on the type of chemical model coupling, the implications are different. There exist essentially two methods for dynamical coupling. One is the (offline) chemical transport model (CTM) approach which bypasses the meteorological time discontinuity by using an temporal interpolation between meteorological analyses, and the other is initialization of the meteorological forecast with the analysis, and then allowing this forecast to drive the chemical model. This is done with dynamically coupled meteorology-chemistry models. Specifically:

(CTM) With an *offline* chemical transport model (CTM). Meteorological analyses which are usually produced at regular time intervals, e.g., 6 h, can be linearly interpolated in time to drive an offline CTM at each time step. This is usually done by interpolating the horizontal wind, temperature and surface pressure and diagnosing the vertical motion from the divergence of the horizontal wind. Alternatively, the vertical motion can also be computed from the diabatic heating rate, giving the vertical motion in isentropic coordinates [77,78], or

(MR) With a coupled dynamical meteorology-chemistry model using *meteorological refresh* (MR). In this case, the coupling is achieved by a direct insertion of meteorological analyses at analysis time. As new analyses are available (e.g., each 6 h), the meteorological variables of the coupled model are reset to the given meteorological analysis values, but in between, the internal dynamics of the coupled model come from the meteorological driver.

Please note that there is also a variant to these approaches, called specified dynamics [7,21] (discussed in the Introduction) that combines the linear interpolation between analyses to force incrementally the dynamical fields of a dynamically coupled meteorology-chemistry model, and thus inherit the properties of both approaches.

CTM coupling has the *advantage* that there is no discontinuity of the meteorological variables at the analysis times. There is a smooth transition of the meteorology from one meteorological analysis time to the next one. However, because of interpolation in time it has the *disadvantage* that meteorology is not dynamically consistent between analyses.

The MR mode has the advantage and disadvantage interchanged compared to those of the CTM mode. It has the *advantage* that during the model time integration between analyses, the meteorology is dynamically consistent. But it has the *disadvantage* that at the analysis time, there is a discontinuity in the meteorological fields, where the jump is a result of the (meteorological) analysis increment.

Table 2 summarizes how meteorology is effectively used in CTM and MR modes.

Table 2. Effective use of meteorology in CTM and MR modes.

	CTM	**MR**
At analysis times	Continuous meteorology	Discontinuous meteorology
Between analysis times	Dynamically inconsistent	Dynamically consistent

For either CTM or MR modes, it is important to note that since there is no chemical data assimilation, the chemical concentrations are time-continuous (both at the meteorological analysis time and between analyses). The absence of changes of concentrations immediately before and immediately after a meteorological analysis time t_A, can be written as

$$\chi(t_A^-) = \chi(t_A^+). \tag{17}$$

However, the time derivative of the concentration at the analysis time t_A is given by

$$\left.\frac{d\chi}{dt}\right|_{t_A^+} - \left.\frac{d\chi}{dt}\right|_{t_A^-} = [\mathbf{V}(t_A^+) - \mathbf{V}(t_A^-)] \cdot \nabla\chi(t_A) = \begin{cases} 0 & \text{CTM mode} \\ \Delta\mathbf{V}^A \cdot \nabla\chi(t_A) & \text{MR mode} \end{cases} \tag{18}$$

where $\Delta\mathbf{V}^A$ is the wind (or meteorological) analysis increment (see Appendix D for a derivation). The time derivative of the concentration is continuous in CTM mode but discontinuous in MR mode.

Let us now outline some properties of the concentration error. In principle, the accumulation of concentration error can be decomposed into two parts: 1—the accumulation of error between the (meteorological) analyses, and 2—an error at the (meteorological) analysis time. However, since the concentration is time-continuous at analysis time (Equation (A9)), and since the true concentrations should also be continuous, we conclude that the concentration error is continuous at the meteorological analysis time (and of course also between meteorological analyses). Thus, in both CTM and MR modes there is no jump in the concentration error at the (meteorological) analysis time. Also, since the meteorological analysis increment is the same in both CTM and MR experiments, the concentration correction (which can be viewed as an unobserved variable in Equation (5), Part II [1]) should also be the same, provided that the error statistics are the same. We thus conclude that any change in concentration error between CTM or MR modes depends essentially on the error in transport between the meteorological analysis times.

We will present in the following section a comparison of experiments using the CTM and MR modes. However, we can already speculate that the use of linearly interpolated winds (as in CTM mode) would create larger transport (concentration) errors than would a dynamically evolving wind field from a coupled meteorology-chemistry model. Thus, we anticipate that concentration errors in MR mode will be smaller than in a CTM mode. The impact of discontinuity in meteorology and dynamical inconsistency is investigated numerically in Section 5.

5. Comparison between CTM and Coupled Meteorology-Chemistry Model

The distribution of atmospheric constituents is strongly driven by photochemistry, emissions and meteorology. For this reason, chemical models driven by meteorological analyses can, to a certain degree, simulate observed concentrations at their proper time and location. In terms of chemistry such simulations are free model runs, while the constraints arising from observations come only from the meteorological analysis.

Meteorological analyses extending to the stratosphere were obtained for the first time under this study (at the time the experiments were carried out, the operational model GEM had a lid at 10hPa only). They were obtained from the CMC 3D-Var-FGAT [55] (i.e., 3D-Var with First Guess at Appropriate Time) and 4D-Var [56] assimilation systems using the tropospheric meteorological observations used operationally at CMC (see [55] Appendix B) and AMSU-A channels 11-14 for the stratosphere using the same bias correction scheme as for tropospheric radiance observations [79] (a procedure also described in Section 4 of [80]). Please note that an improved bias correction will be presented in Part II [1] Section 4.

Several experiments were carried out to quantify the different sources of errors between GEM-BACH in MR mode and the BASCOE CTM. All MR experiments were performed at $1.5^\circ \times 1.5^\circ$ resolution, i.e., 240×120 grid points, with 80 levels (27 levels are in the stratosphere) and a 45 min timestep as described in Section 3.1. In the case of the CTM experiments the same horizontal and vertical resolution were used but with a timestep of 15 min because its flux-form semi-Lagrangian requires satisfying the Courant-Friedrichs-Lewy condition in the meridional direction. All experiments were evaluated over a period of 12 days in late summer 2003.

Figure 6 shows the results of an ozone simulation for CTM and MR modes using different meteorological analyses. The comparison is made against limb sounding ozone observations from the Envisat/MIPAS instrument. The solid lines depict the mean difference, and the dashed curves the standard deviation. The dashed curves are plotted symmetrically with respect to the zero error (vertical solid black line), simply to illustrate the range of $\pm\sigma$ random errors. Also note that all the errors are normalized by the observed values, so that the errors are expressed as a percentage. The differences are computed from interpolating the model values to the observation location, at the observation time of validity. We emphasize that the chemistry model is the same in all experiments, and the results differ only due to the meteorological analysis and its coupling to the chemistry transport. The red and grey curves are results from using MR (meteorological refresh) mode using the CMC 3D-Var-FGAT and 4D-Var meteorological analyses respectively, while the green curves are results based on the CTM mode using 3D-Var-FGAT analyses.

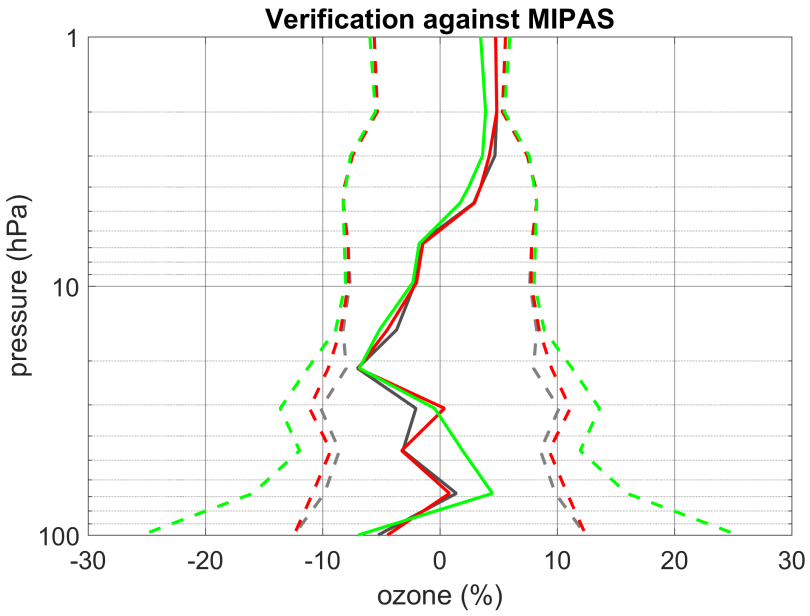

Figure 6. CTM coupling vs. MR. Solid curves are mean observation-minus-model differences of O_3, and dashed curves are error standard deviations. The grey curves correspond to the MR mode using CMC 4D-Var meteorological analyses, the red curves correspond to the MR mode using the CMC 3D-Var-FGAT analyses. The green curves correspond to the CTM mode of coupling using the CMC 3D-Var-FGAT analyses.

First, we draw the reader's attention to the error standard deviation (i.e., dashed curves). We note that between 100 hPa and 20 hPa where the photochemical timescale is of the order of several months (i.e., transport is dominant), the standard deviation is significantly larger with the CTM mode and reaches twice the MR values at 100 hPa. The difference between red and green curves is only due to the mode of coupling, CTM vs MR. Also, there is little difference between using 3D-Var-FGAT and 4D-Var meteorological analyses. The main difference arises from whether the MR mode or CTM mode is used. This indicates that the dynamical inconsistency in the time integration window of 6 h is the main source of random error, while using different analyses is of secondary importance.

Similar conclusions can be drawn for the systematic error (solid curves), where we observe that the main difference in error arises from using either MR or CTM mode of coupling rather than using different meteorological analyses (either 3D- or 4D-Var).

Above 20 hPa, where the photochemical timescale is shorter and transport plays a negligible role with respect to photochemistry, there is no difference in error standard deviation but only a slight difference in systematic error, probably due to differences in mean temperatures between the different meteorological analyses.

These results clearly indicate that despite the jump in the wind field at the analysis refresh time, the integration consistency which arises in coupling with MR gives a superior chemistry simulation compared to the time interpolation error and associated dynamical inconsistency in CTM coupling. We conclude that for chemical data assimilation, model error due transport is smaller for coupled models in MR mode compared to offline models in CTM mode.

6. Discussion on the Use of Lower Resolution

It has been argued that the tracer distribution is primarily controlled by the large-scale low-frequency component of the flow [31] and thus, a lower-resolution meteorology could be used in a chemical transport model, and yet produce realistic simulations. A similar argument exists for

meteorological data assimilation, where lower-resolution analysis increments produced in a 4D-Var scheme (i.e., incremental 4D-Var) are able to create realistic small-scale structures over time through the atmospheric model [81,82]. The arguments presented for both tracer-wind transport and the incremental 4D-Var are based on models that are dominated by an enstrophy cascade with a k^{-3} spectrum, where k is the wavenumber. Large-scale lower-resolution atmospheric and barotropic vorticity models exhibit such behavior—the sources of energy injected at small wavenumbers cascade down to higher wavenumbers. Nevertheless, in the stratosphere, as simulated by high resolution meteorological models, energy spectra evolve from a steep spectrum, $\propto k^{-3}$, to a shallow spectrum as the height increases [83] resulting from an inverse energy cascade $\propto k^{-5/3}$ at larger wave numbers. We thus expect that GEM-BACH has a similar behavior.

The chemical tracer field has what is called a scalar variance spectrum that has in theory a slope lying between -1 for enstrophy-cascade dynamics to $-5/3$ for inverse energy cascade dynamics [84]. However, because of mixing barriers and trapping by persistent vortices, it has been argued that the scalar spectral slope can be as steep as -2 in those cases [85]. However, in general, stratospheric observations indicate that slopes of $-5/3$ in the scalar variance are usually obtained [86,87].

In the context of tracer-wind transport, the argument that low-resolution winds can reproduce the small-scale structure of tracer fields has been challenged by Bartello [84]. He pointed out that lower-resolution models dominated by enstrophy-cascade dynamics can reproduce accurately some fine structure of the tracer field [84,88] using a relatively coarse wind field. However, higher-resolution models, with an inverse energy cascade at smaller scales, create fictitious small-scale structures in the tracer field when coarse resolution winds are used [84].

These results are of direct relevance to coupled stratospheric chemistry–meteorology modeling and data assimilation. In the stratosphere, where the inverse energy cascade is important, the use of lower-resolution analysis increments, e.g., incremental 4D-Var, is expected to result in a loss of information in the stratospheric meteorological analysis. Furthermore, chemical tracer fields driven by lower-resolution analysis increments would also lose accuracy in small-scale structures. For these reasons, we argue that for stratospheric models such as GEM-BACH, we should generate analysis increments at the same resolution as the meteorological model, and also drive the chemistry at the same resolution as the meteorological model, so as not to introduce small-scale errors in both meteorology and chemical tracer fields.

Bartello [84] also noted that the temporal resolution of the advecting velocity would have a timescale $\propto k^{-2/3}$ and thus an increase in spatial resolution requires a corresponding increase in temporal sampling. Linear time interpolation used in CTM's would then be detrimental, which has been clearly identified in Section 5.

To illustrate our discussion regarding resolution, we have chosen an ozone depletion event and conducted a few experiments over the period August–October 2003. First, we have conducted a 3D-Var-FGAT meteorological assimilation with GEM at $1.5^\circ \times 1.5^\circ$ resolution producing analysis increments at the same resolution, and driving the coupled model GEM-BACH in the MR mode also at the same resolution. The choice of the horizontal resolution (i.e., $1.5^\circ \times 1.5^\circ$) is guided by the ability to accurately model the ozone hole. We remark that many successful studies of polar ozone depletion use CTM or specified dynamics GCCM with latitude–longitude resolutions of approximately $2^\circ \times 2.5^\circ$ [22]. This resolution became typical for GCCM aiming at modeling the ozone hole as the minimum resolution allowing a realistic representation of the tropical and high-latitude mixing barriers (i.e., polar vortex edges) [89]. It should also be noted that several modeling groups use even coarser resolutions to model polar ozone depletion, e.g., with a 3-D CTM at $2.5^\circ \times 3.75^\circ$ [90] or with a chemistry climate model in nudged (SD) mode at T42 (i.e., approximately $2.8^\circ \times 2.8^\circ$) [91]. Hence the choice of $1.5^\circ \times 1.5^\circ$ was deemed sufficient to accurately model the ozone hole with GEM-BACH.

Figure 7 panel (a) shows the total column ozone measurements from the TOMS instrument on 30 September 2003. Typical to such events, we note there is a wide range of total ozone amounts (and thus of ozone concentration values) and sharp gradients along the vortex edge. The results of pure

chemical simulation with MR and at the resolution 1.5° × 1.5° are presented in panel (b) of Figure 7. We observe a remarkably accurate simulation of the ozone depletion event, with accurate vortex values, sharp gradients along the vortex edge and reasonably well-reproduced mid-latitude surf-zone values. Tropical values (see Figure S12 in Supplementary Material) are lower than observed (we know from Section 7.2.3 that the GEM-BACH model has an ozone deficit problem). Nevertheless, this represents a major accomplishment, taking into account the fact that there is no chemical assimilation in this run.

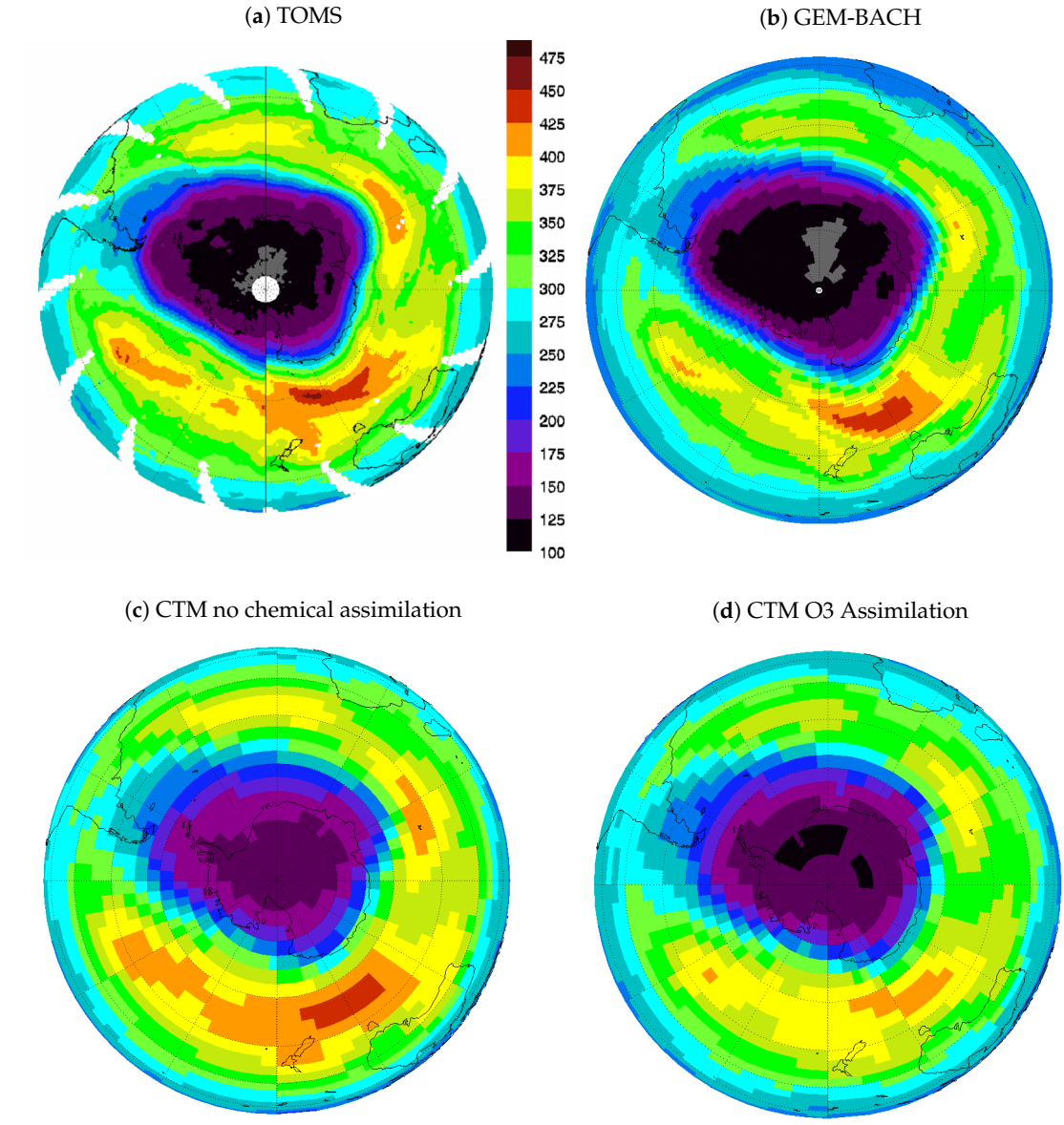

Figure 7. Total column ozone (DU) for 30 September 2003. Panel (**a**) Observations from TOMS (v7). Panel (**b**) GEM-BACH refreshed with the Canadian 3D-Var-FGAT analysis. Panel (**c**) CTM in low-resolution mode (3.75° × 5°). Panel (**d**) BASCOE 4D-Var assimilation of ozone MIPAS (ESA) observations. Grey areas represent pixels where the ozone column is smaller than 100 DU.

We now compare the BASCOE CTM (panel c) and 4D-Var chemical data assimilation (panel d), as is done operationally at BIRA, using the operational ECMWF meteorological analysis. Since 4D-Var chemical assimilation is costly, the model and assimilation are performed at a lower resolution, in the case here both at 3.75° × 5°. As in GEM-BACH, heterogeneous chemistry is simulated using prescribed climatological SAD values (see Section 3.2). The CTM simulation with the coarser-grained model

overestimates both the vortex and mid-latitude surf-zone values and has weak gradients at the vortex edge. Thus, it appears that lower-resolution winds driving a chemical model at the same resolution cannot reproduce the sharp gradients (i.e., small-scale structures in the chemical field) at the vortex edge. Although this result is simply an illustration, it does not support the claim that the large-scale, low-frequency component of the flow controls the tracer distribution. It is important to note that both the BASCOE CTM and GEM-BACH have no horizontal diffusion that could smooth horizontal gradients. Any horizontal gradient or lack thereof is a result of the driving winds and underlying cascade regime.

Next, 4D-Var assimilation of ozone observations from MIPAS was conducted with a low-resolution BASCOE 4D-Var assimilation system and the result is presented in panel (d). We note lower ozone values in the polar vortex than with the BASCOE CTM at the same low resolution (panel c), but the horizontal extent of these low values (column < 125 DU) is not as large as in TOMS observations (panel a). The extent of the depleted area is actually better simulated by the higher-resolution GEM-BACH model (panel b) then by this MIPAS-based analysis (panel d), where we also observe a weakening of the concentrations outside the polar vortex. This is apparently an effect of the error covariances and the impact of observations near the vortex edge that tend to mix values in and out of the vortex, which can be partly alleviated if a more appropriate covariance model is used [92].

These results argue in favor of using the same resolution for both meteorological and chemical components, as well as analysis increments. Combined with the selection of the Meteorological Refresh mode (see previous Section 5), this provides the justification for the data assimilation setup used in the next Section 7 and in Part II [1].

7. Evaluation of GEM-BACH Driven in Meteorological Refresh (MR) Mode

7.1. MIPAS and HALOE Measurements

The MIPAS instrument on-board the Envisat satellite [93] is a limb sounder which uses a Fourier-transform spectrometer for the detection of emission spectra in the middle and upper atmosphere [93–95]. It observes a wide spectral interval throughout the mid-infrared with high spectral resolution, which permits retrievals of pressure in addition to temperature and volume mixing ratio (VMR) of different gases. The instrument provides about 1000 profiles per day (day and night) with a global spatial coverage. The operational ESA retrievals v4.61 that we used here do not use any *a priori* and thus can be considered to be "pure observations". The typical root mean square error (RMSE) observation error of MIPAS is about 2° K for temperature [96], 10% VMR error for O_3 [97], 20% VMR error for H_2O, CH_4 and N_2O [98,99]. Other species such HNO_3 and NO_2 have a large relative error that varies considerably with altitude (although with a minimum error of 10% at 22 km for HNO_3 and at 40 km for NO_2) [100,101] and were used in this comparison.

The HALOE instrument on-board the UARS satellite [102–104] is a solar occultation instrument which employs a broadband radiometer, and a gas correlation technique specifically to infer aerosol extinction [105]. Each HALOE radiometric profile is divided by the exo-atmospheric signal thus giving a direct measurement of the atmospheric transmission for each channel. HALOE retrieves temperature and mixing ratio of several species. The horizontal coverage is limited to two latitudes on a given day, one at sunrise and the other at sunset. These sun occultation latitudes change gradually over a period of 45 days, as the UARS satellite is on an inclined orbit and undergoes precession. The whole latitudinal coverage is quite complicated but ranges from ∼45° in one hemisphere to ∼80° in the other hemisphere. Every 45 days the hemispheric coverage is inverted through a yaw maneuver of the satellite. The HALOE retrieval of atmospheric constituents is a modified "onion peel" algorithm with no a priori information. The main source of error arises from the absence of pressure measurements. Because of the pointing uncertainty, there is a need to perform a registration of profiles with altitude and pressure, which is done by referencing a meteorological analysis that contains errors [104]. HALOE

retrieval V19 used in this study is considered an excellent verification dataset with errors less than 10% for ozone, temperature and H_2O [105–107] and 15% for CH_4 [108].

7.2. GEM-BACH Evaluation against Satellite Observations

Data assimilation schemes are based on the assumption that errors (model and observations) are random rather than systematic. These (first) evaluations were performed, in part, to establish the readiness in assimilating MIPAS observations, by assessing whether the differences between the model and observations is dominated by random errors rather than biases.

7.2.1. Temperature

Temperature is important for the chemistry and for the thermal–wind component of the transport. Figure 8 shows the difference between temperature observations and GEM-BACH driven in MR mode (positive differences correspond to observed values being larger than modeled values). Results using MIPAS are displayed in the left panel and HALOE in the right panel. The statistics (mean and standard deviation) use model values interpolated to the proper time and location of the individual observations. The verification results indicate a good agreement for temperature below 10 hPa and a relatively warm bias above. Since the warm bias between 0.4 and 10 hPa is similar for both MIPAS and HALOE, we conclude that the bias is due to the model or the meteorological analysis that drives GEM-BACH. Also, we should note that for this two-month period (1 August to 30 September 2003), the horizontal coverage of the two instruments is not the same. HALOE is limited to the band 40° S to 70° N for this time period.

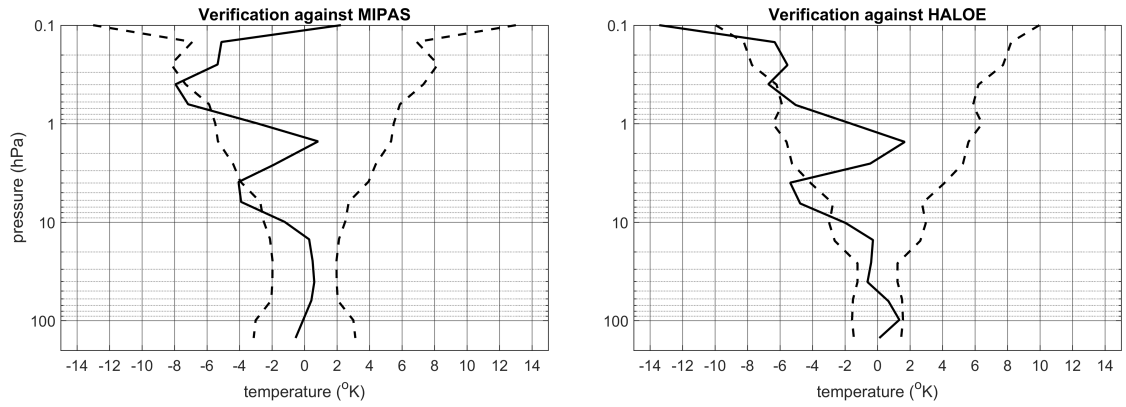

Figure 8. Temporally (August–September 2003) and globally averaged temperature differences between MIPAS and GEM-BACH (**left panel**) and HALOE and GEM-BACH (**right panel**) as a function of height (in hPa). The solid lines are the mean difference and the symmetric dashed curves are the standard deviation. Observation-minus-model are in degree K.

The agreement in temperature below 10 hPa indicates that MIPAS temperatures are likely to be in agreement with radiosonde temperatures assimilated in GEM-BACH. Indeed, radiosondes measure temperature up to 30 hPa (in the tropics), but their effect on meteorological analyses can be observed up to about 10 hPa. Since radiosonde temperatures provide a strong constraint on meteorological analyses, they have a (significant) impact on GEM-BACH in the MR mode. Thus, the agreement with MIPAS temperatures below 10 hPa, as seen Figure 8, is an indication of agreement with radiosonde temperatures. Lastly, since we are specifically interested in temperatures over the polar region for heterogeneous chemistry, Figure S7 shows good agreement over the South Pole region (between 70° S and 90° S) during the month of August (important for the onset of ozone hole events).

7.2.2. Methane and Nitrous Oxide

Continuing our assessment of meteorology, evaluation of the distribution of long-lived species, in particular CH_4 and N_2O, can provide information about the quality of the wind fields. The evaluation of CH_4 against MIPAS and HALOE observations is presented in Figure 9. It shows that the model CH_4 is in good agreement with MIPAS observations across the entire stratosphere.

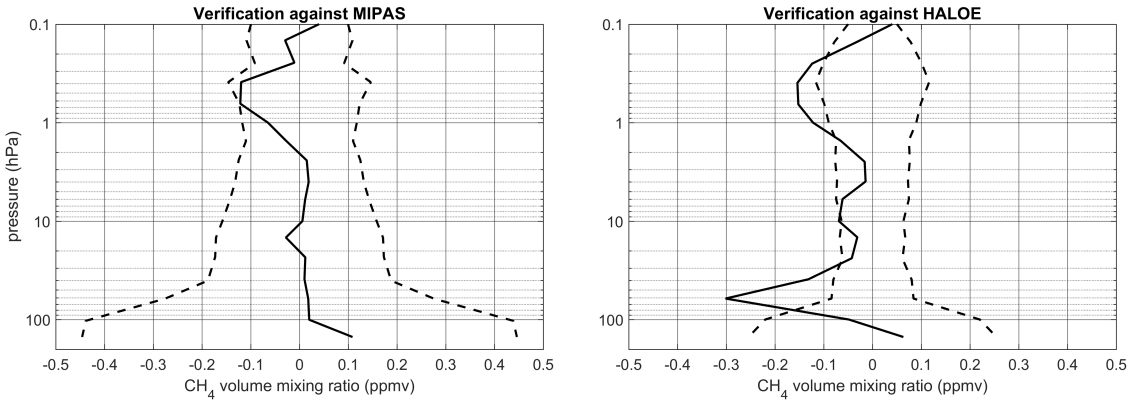

Figure 9. Temporally (August–September 2003) and globally averaged volume mixing ratio (ppmv) differences between satellite measurements and GEM-BACH modeled CH_4. Observation-minus-model values are in ppmv. The solid lines are the mean difference and the symmetric dashed curves are the standard deviation.

Also, remarkable agreement with MIPAS measurements of N_2O is observed (see Figure S8 in Supplementary Material). These results indicate that the wind fields produced by the meteorological analysis (in MR mode) are of good quality in the stratosphere. However, the comparison with HALOE CH_4 measurements shows non-negligible biases both in the lower and upper stratosphere, although the standard deviation is small, indicating that the spatial patterns in the modeled distribution of CH_4 remain close to the observations.

The fact that accurate winds can be obtained in the stratosphere deserves some attention. We recall that GEM-BACH is driven in MR mode. The meteorological analyses are affected by wind observations only from the troposphere. In the stratosphere, temperature-sensitive radiance observations are the main source of observations. Although satellite radiance observations often have an offset and may result in temperatures being inaccurate (even after the radiance bias correction), we can argue that the horizontal distribution of radiances is well captured, and consequently the horizontal temperature gradient is well represented. It is known that for the most part, on synoptic timescales, the stratosphere is in geostrophic balance (and, on large scales, in gradient-wind balance) as discussed in Section 2.2. Thus, we argue based on the thermal–wind relation Equation (3) that the vertical shear of the geostrophic wind in the stratosphere is also well captured since the horizontal gradient of temperatures is reasonably captured by the stratospheric meteorological analyses. The tropospheric winds are also well represented in tropospheric meteorological analysis. Thus, using these winds as the lower boundary condition in the thermal–wind Equation (3), we can deduce the 3D-distribution of the geostrophic wind in the whole stratosphere. This makes the point that the stratospheric winds are well represented. Lastly, since the wind field and tracers are closely related as a result of shear flow balanced by stirring and mixing, as discussed in Section 2.3, we can understand that the distribution of long-lived species is also well captured throughout the stratosphere with a coupled model driven in MR mode.

It is also useful to compare the verification by region (Tropics vs. South Pole) for the long-lived species CH_4 and N_2O. In an experiment where we gathered the data over the period of 17 August to 7 September 2003, we plotted the relative error (which is dimensionless, rather than the volume

mixing ratio) for two regions, the tropics (from 30° S to 30° N) and over the South Pole (south of 60° S). The results are shown in Figure 10.

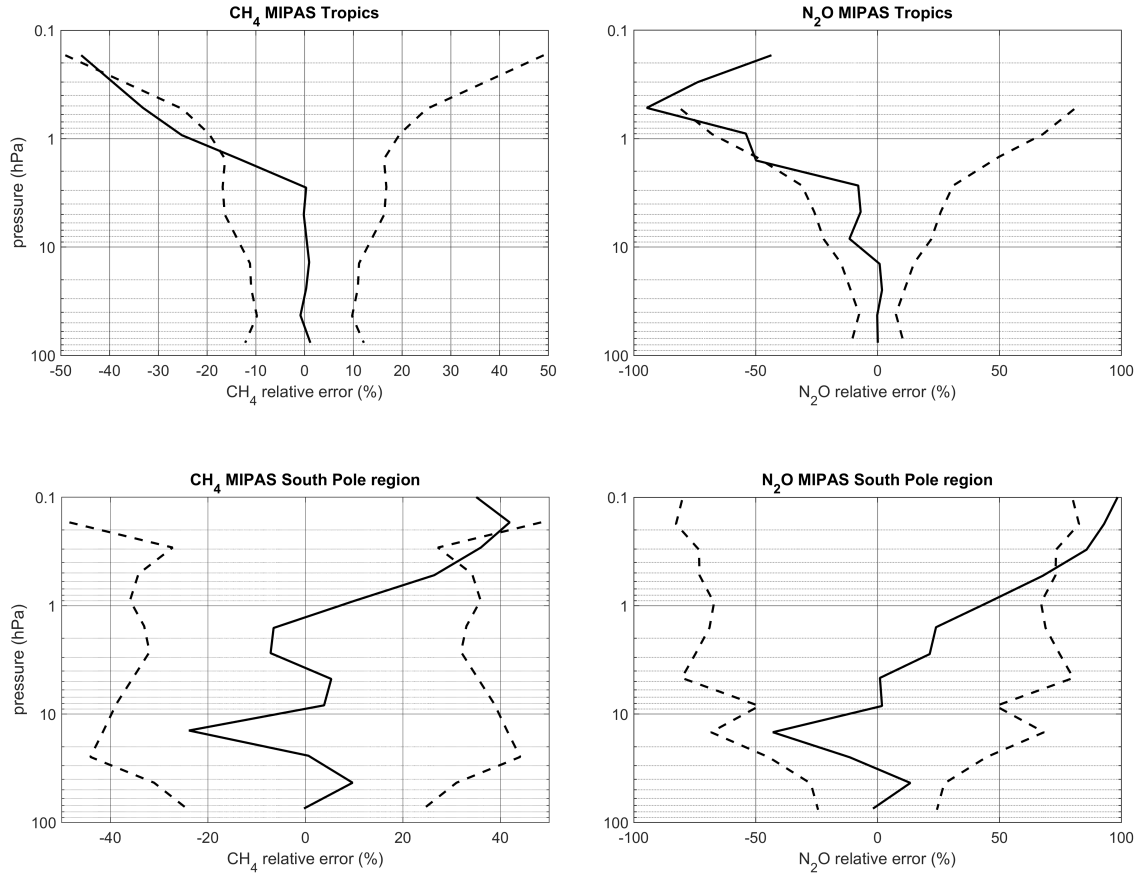

Figure 10. Averaged relative error differences between MIPAS measurements and GEM-BACH modeled for CH_4 and N_2O over the tropics and over the South Pole region. The solid lines are the mean difference and the symmetric dashed curves are the standard deviation.

We note that above 3 hPa both modeled values for CH_4 and N_2O are overestimated in the tropics, and inversely, the modeled values are underestimated over the South pole region, whereas there is little bias below 3 hPa in the tropics. Since both species are chemical tracers, the effect presented is primarily due to transport, and is similar for each species. These results suggest that above 3 hPa the equator-to-south pole portion of the Brewer–Dobson circulation is too weak in the model, and thus compared with observations the modeled values are too small in the tropics and too large on the other extreme of the Brewer–Dobson circulation over the South Pole region.

7.2.3. Ozone and Water Vapor

Important meteorological-chemical interaction arises with gases such as O_3 and H_2O. Global averages of O_3 differences for the period of August-September 2003 are presented in Figure 11. We observe a significant model ozone deficit (i.e., underestimation) in the upper stratosphere with a maximum deficit of about 15% at 0.7 hPa. This can be explained, at least in part, by the model warm bias at these altitudes and the negative correlation between temperature and ozone, as explained in Section 2.1, in particular, making use of Equation (2). The model ozone deficit in the upper stratosphere may also be partly due the severe overabundance of model NO_2 in the upper stratosphere (see Figure S9 in Supplementary Material), since nitrogen dioxide, NO_2, catalytically destroys ozone. The model's overestimation of NO_2 is also supported by the comparison of GEM-BACH against

Fourier-Transform InfraRed (FTIR) spectrometer measurements at Eureka [109] (see also Section 7.3). A better agreement between GEM-BACH and HALOE in terms of O_3 is observed from 2 to 10 hPa, and with an overestimation below 10 hPa. This positive bias in GEM-BACH simulations is also seen when we compare the model against ozone sondes (displayed in Figure S10, Supplementary Material). The above considerations indicate that around 30 hPa GEM-BACH globally averaged O_3 concentrations are too high and that HALOE observations are more accurate than MIPAS ESA retrievals. However, over the South Pole region, Figure 12 shows that GEM-BACH concentrations match the MIPAS concentrations between 3 and 30 hPa, the region of ozone destruction.

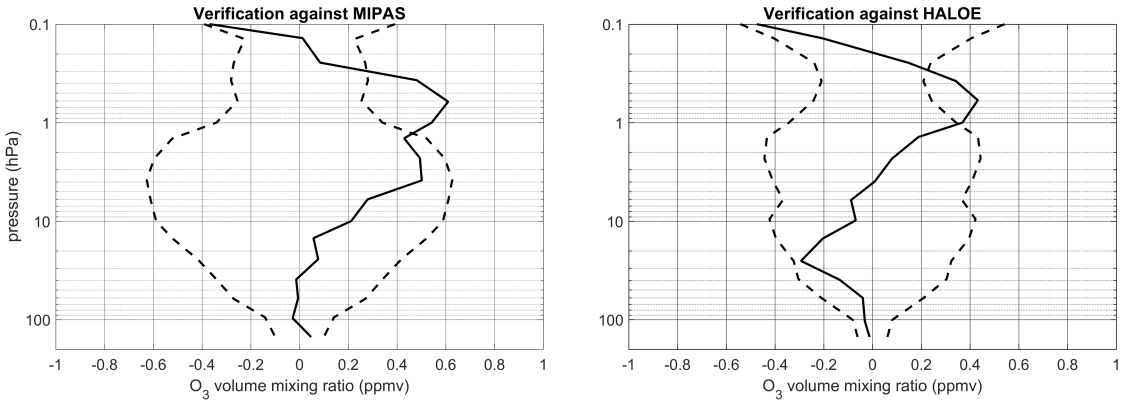

Figure 11. Temporally (August–September 2003) and globally averaged volume mixing ratio (ppmv) differences between satellite measurements and GEM-BACH modeled O_3. Observation-minus-model values are in ppmv. The solid lines are the mean difference and the symmetric dashed curves are the standard deviation.

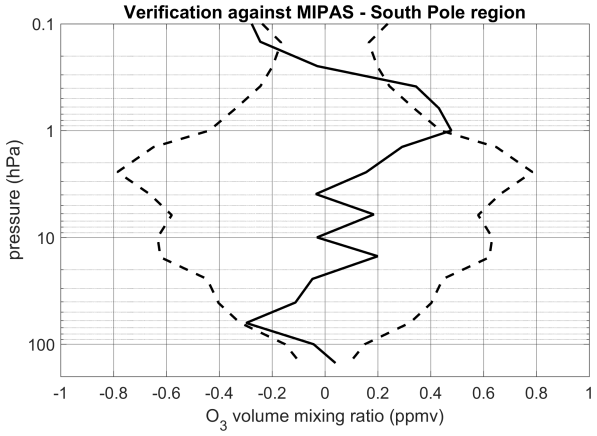

Figure 12. Monthly (August 2003) averaged volume mixing ratio (VMR) differences in O_3 between MIPAS and GEM-BACH over the South Pole region as a function of height (in hPa). The solid lines are the mean difference and the symmetric dashed curves are the standard deviation.

Water vapor plays an important role in the ozone budget at the stratopause. It has an important radiative impact in the lower stratosphere/tropopause region. A comparison of GEM-BACH H_2O against MIPAS and HALOE profiles is presented in Figure 13. Good of agreement with MIPAS data throughout the stratosphere as well as a model overestimation near the model lid are evident.

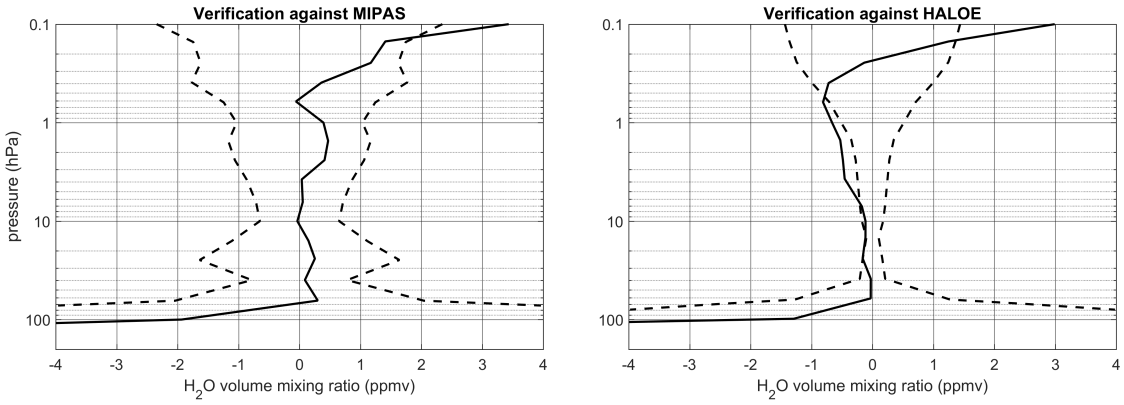

Figure 13. Temporally (August–September 2003) and globally averaged volume mixing ratio concentrations H_2O. The solid lines are the mean difference and the symmetric dashed curves are the standard deviation.

We note that compared with HALOE data, there is a gradual increase in the H_2O bias with height, indicating a positive model bias which grows gradually with height across the stratosphere. Closer to the tropopause, we observe a significant model overestimation compared to both MIPAS and HALOE data. Since the retrieval error is important and the variability of H_2O is very large, a definitive conclusion would require a more detailed investigation, which we have not carried out here. In fact, since there is a sharp transition in H_2O at the tropopause and because the tropopause height varies considerably between the tropics and the polar regions, the global average is simply not a good comparison statistic.

7.3. GEM-BACH Evaluation against Ground-Based Total Column Measurements

An evaluation of stratospheric trace-gas column distribution in GEM-BACH was made against the Network for the Detection of Atmospheric Composition Change (NDACC) Bruker 125HR FTIR spectrometer data at Eureka (Eureka, Nunavut, Canada (80.05°N, 86.42°W)). The comparison was carried out during the International Polar Year (IPY), from 1 March 2007 to 28 February 2009 and the data are publicly available on the SPARC-IPY web site [110].

The FTIR instrument, retrieval methods and measurements during this time are described in depth in Batchelor et al. [111,112]. While an additional comparison between this FTIR and GEM-BACH and other models for the NOy budget has been published by Lindenmaier et al. [109], it is valuable to provide an example of how GEM-BACH compares with ground-based measurements as part of this discussion, especially for O_3, HCl and CH_4 which were not examined in [109].

Comparisons between the FTIR stratospheric partial columns measured at Eureka for six chemical species during 2007 are shown in Figure 14. Here the GEM-BACH model is refreshed with CMC meteorological 3D-Var-FGAT (First Guess at Appropriate Time) analyses every 12 h. The configuration of GEM-BACH is identical to that described in Section 3 except that the surface area density for the PSC's has been reduced to provide a better agreement with ozone observations in polar regions.

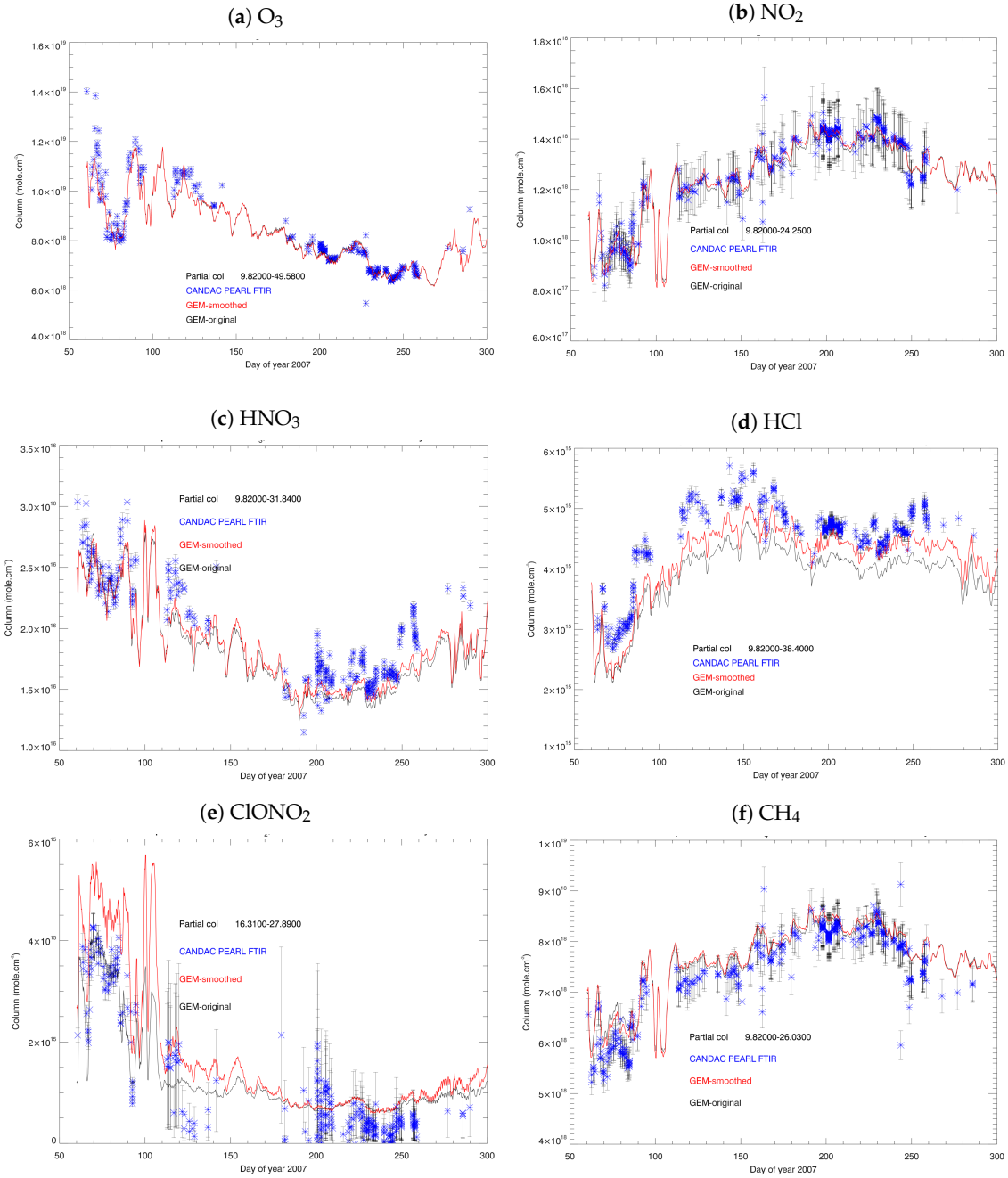

Figure 14. Lower stratospheric partial columns of O_3, NO_2, HNO_3, HCl, $ClONO_2$, and CH_4 (left to right, top to bottom) as observed by the FTIR spectrometer at Eureka (blue stars and black error bars) compared with the same partial columns determined from the GEM-BACH simulation before (black line) and after (red line) vertical smoothing based on averaging kernels and a priori of the FTIR retrieval. The pressure bounds for the partial column differ for each species (see plot inset; units are in hPa) to select the vertical range where the sensitivity of the FTIR is > 0.5.

As described in [111,112], the vertical resolution of the FTIR measurements is limited, and in some parts of the atmosphere the a priori contributes significantly to the column. To account for this and provide a clean comparison, the higher-resolution GEM profile χ_m is smoothed with the FTIR a priori χ_a and averaging kernel $\mathbf{A}$, to provide a smoothed profile χ_s as defined in [113],

$$\chi_s = \chi_a + \mathbf{A}(\chi_m - \chi_a). \quad (19)$$

The column is determined from the smoothed profile, with the partial column bounded between 9.8 hPa (corresponding to approximately the bottom of the stratosphere) and the maximum altitude where data contributes more than the a priori (sensitivity > 0.5) to the FTIR retrieval. The argument to use Equation (19) can be understood from the fact that if we replace χ_m by the true concentration χ, we get the standard expression for a retrieved profile using the averaging kernel **A**. Then, with the ansatz that GEM-BACH provides an ideal high resolution profile, if we substitute it for the truth, we then get a smoothed or equivalent "retrieved" profile [113] that we can compare with the FTIR retrieval.

Observations at Eureka provide a usefully challenging test case for modeling, with the dynamic polar vortex allowing air inside, through the edge, and outside of the vortex to be sampled overhead. Figure 14 demonstrates how well GEM-BACH captures this dynamical variability. Between day 65 and 85 of the SPARC-IPY campaign, the FTIR sampled the air mass inside the polar vortex, as seen in the perturbed profile across all the gases. The 2006/2007 polar winter was characterized by a strong, cold polar vortex with significant amounts of ozone depletion [114,115]. This is well captured in the model, with ozone (panel (a)) tracking the FTIR columns extremely closely, both inside and outside the vortex. The day-to-day dynamic and seasonal variability is captured throughout the year across all gases, suggesting that both meteorological and radiation processes are being captured well. As described in [109] there are some consistent offsets seen between the model and data in the chlorine reservoir species HCl and $ClONO_2$, and in HNO_3 (though the latter matches well within the 2007 vortex, GEM-BACH is typically 10% lower than observed throughout the rest of the comparison period [113]). These differences are likely due to not including all of the chlorine sources (CFCs), as well as limitations in the PSC treatment, which is tuned to Antarctic conditions and does not include type 1b liquid PSC particles, which play a bigger role in the Arctic [113].

Methane (CH_4) is an important greenhouse gas, and several recent studies have focused on better understanding the contribution of the stratosphere to the methane column [116,117]. Figure 14 panel (f) shows a seasonal bias in the modeled stratospheric CH_4, with excellent agreement in the summer and a high bias in the spring and fall. A similar overestimation of CH_4 at high northern latitudes is observed and the cause remains a subject of investigation.

8. Summary and Conclusions

A fully coupled meteorology-chemistry model, called GEM-BACH, was developed by combining the stratospheric extension of the NWP model GEM with the BASCOE chemical transport model using a chemical interface that preserves time-splitting properties while being modular, allowing the system to run with or without chemistry. The increase in computational cost was minimal due to the semi-Lagrangian scheme where the upstream point and interpolation weights are computed only once for all species.

The project started with a preliminary stratospheric version of the CMC operational meteorological model GEM [57], where the non-orographic gravity wave drag [39,40] and a k-correlated radiative schemes [60] were added. The model then produced realistic lower stratosphere temperatures over the South Pole for the initiation of PSC chemistry, and with a prescribed Stratospheric Sulfate Aerosol (SSA) surface area densities gave rise to realistic simulation of the ozone hole without chemical data assimilation (but driven by meteorological analyses), a rare outcome for a pure simulation (Guy Brasseur, personal communication).

We compared chemical observations with GEM-BACH simulation in which with the meteorology component was replaced by meteorological analysis every 6 h. This mode of coupling with meteorological analyses was called meteorological refresh (MR) mode, and the accuracy of the simulated chemistry was compared with the standard CTM approach, where an offline chemistry model is driven by meteorological analyses linearly interpolated in time. The results show that the dynamical consistency provided by the coupled model driven with meteorological analysis refresh (MR), although with an offset created every 6 h by the meteorological analysis, is much more accurate than a linear interpolation of analyses used to drive an offline CTM. This conclusion was reached

irrespectively of the type of meteorological analysis used, whether it came from a 3D-Var or a 4D-Var assimilation scheme.

We also add a discussion on the importance of having (relatively) high resolution meteorological analyses and analysis increments computed at the same resolution as in the coupled model. The GEM-BACH simulation of the ozone hole event of 2003, with the coupled model driven in MR mode, gave particularly good results compared with independent observations, in terms of values inside and outside the vortex, as well as the gradient along the vortex edge. The quality of the 4D-Var ozone assimilation performed with a CTM at much lower resolution did not approach the simulations with GEM-BACH, thus stressing the importance of resolution in obtaining accurate chemical fields.

The temperature in GEM-BACH, driven in MR mode with the standard meteorological observations showed fairly good agreement (in the lower stratosphere) with independent temperature measurements from MIPAS and HALOE. But large and similar biases against MIPAS and HALOE were observed in the middle and upper stratosphere, indicating a warm bias in either GEM or in the standard meteorological temperature data. On the other hand, the quality of the transport, evaluated by comparing the model output to observations of long-lived chemical species, showed good quality throughout the stratosphere, both in a global time-averaged mean and in their daily variability, compared with total column ground-based FTIR measurements. However, the model upper stratospheric ozone is underestimated by the BASCOE chemistry, which may be attributable to temperature overestimation or poorly modeled NOx at these altitudes. Rather good agreement was observed with chemically produced H_2O throughout the stratosphere.

Supplementary Materials: The following are available online at http://www.mdpi.com/2073-4433/11/2/150/s1, Figure S1: Vertical distribution of solar short wave heating rates and long wave cooling rates; Figure S2: Schematic of the Brewer-Dobson circulation Northern hemisphere winter; Figure S3: Zonal mean temperature for Northern hemisphere winter; Figure S4: Zonal mean wind for Northern hemisphere winter; Figure S5: Time series of zonal wind at the equator; Figure S6: Sulfate aerosols climatology; Figure S7: Monthly average of MIPAS temperature observations minus GEM-BACH values over the South Pole region; Figure S8: Temporal (August-September 2003) and global average of HALOE NO_2 concentration minus GEM-BACH; Figure S9: Temporal (August-September 2003) and zonal average of ozone sonde concentrations minus GEM-BACH; Figure S10: Spatial distribution of ozone sondes of the WOUDC network; Figure S11: Temporal (August-September 2003) and global average of MIPAS N_2O concentration minus GEM-BACH; Figure S12: Total column ozone (DU) for 30 September 2003

Author Contributions: Conceptualization, R.M., S.C.; methodology, R.M., S.C. and M.C.; software, S.C., M.C., Y.R., A.K., A.R., J.d.G., and J.W.K.; validation, S.C., R.B., Y.R. and M.C.; formal analysis, R.M., J.d.G. and S.C.; investigation, S.C., M.C., R.B., A.R., M.R., J.d.G., and J.W.K.; data curation, S.C. and M.R.; writing—original draft preparation, R.M. and S.C.; writing—review and editing, M.R., Y.R., A.K., R.B., J.d.G. and S.C.; visualization, R.M., S.C., A.R. and J.d.G.; supervision, R.M. and S.C.; project administration, R.M.; funding acquisition, R.M. All authors have read and agree to the published version of the manuscript.

Funding: This work was funded by the European Space Agency/ESTEC contract No. 18560/04/NL/FF "Coupled Chemistry-Dynamics Data Assimilation" with the Contract Officer Tobias Wehr (ESA/ESTEC). This work was also supported in kind from the Atmospheric Science and Technology Directorate of Environment and Climate Change Canada (ECCC). The Eureka FTIR measurements were made at the Polar Atmospheric Research Laboratory under the CANDAC project led James R. Drummond, and in part by the Canadian Arctic ACE/OSIRIS Validation Campaigns lead by Kaley A. Walker. Funding was also provided by AIF/NSRIT, CFI, CFCAS, CSA, ECCC,GOC-IPY, NSERC, NSTP, OIT, and ORF. Logistical and operational support was provided by the PEARL Site Manager Pierre Fogal, the CANDAC operators, and the ECCC Weather Station.

Acknowledgments: We wish to thank Saroja Polavarapu for her numerous advice and as the Canadian IPY representative for her help in facilitating the production and storage of the data on the IPY data repository. We wish to thank Kimberly Strong at the University of Toronto as the PI of the FTIR measurements at Eureka, who provided access to the measurement data. We wish thank Michel Béland, Director of Climate and Atmospheric Research Directorate and late Keith Puckett Director of the Air Quality Research Division both Environment and Climate Change Canada for their continuous support in making this project a reality. We thank Dominique Fonteyn from the Belgian Institute for Space Aeronomy for the initiation of our fruitful partnership. We thanks Paul Vaillancourt, Paul André Beaulieu, Sylvain Ménard, Mike Neish and Cathy Xie from ECCC, and late John C. McConnell from York University as well as Quentin Errera from BIRA for their help and advice on specific issues. Finally, we are grateful to Kirill Semeniuk and all the authors for a review of the manuscript, as well as for three anonymous reviewers.

Conflicts of Interest: The authors declare no conflict of interest. The funders had no role in the design of the study; in the collection, analyses, or interpretation of data; in the writing of the manuscript, or in the decision to publish the results.

Abbreviations

The following abbreviations are used in this manuscript:

BASCOE	Belgian Assimilation System for Chemical ObsErvations
BIRA	Belgian Institute for Space Aeronomy
CMC	Canadian Meteorological Center
CRISTA	CRyogenic Infrared Spectrometers and Telescopes for the Atmosphere
CTM	Chemical Transport Model
ECCC	Environment and Climate Change Canada
ECMWF	European Center for Medium-Range Weather Forecasting
EOS	Earth Observing System
ESA	European Space Agency
FGAT	First Guess at Appropriate Time
FTIR	Fourier-Transform InfraRed spectrometer
GAW	Global Atmospheric Watch
GCCM	Global Chemistry Circulation Model
GEM	Global Environmental Multiscale
GEM-BACH	GEM-Belgian Atmospheric CHemistry
GHG	Greenhouse Gas
GMAO	Global Modeling and Assimilation Office
GOME	Global Ozone Monitoring Experiment
GWD	Gravity Wave Drag
HALOE	HALogen Occultation Experiment
IPY	International Polar Year
IR	Infrared
KPP	Kinetic PreProcessor
LINOZ	LINearized model for OZone
MDPI	Multidisciplinary Digital Publishing Institute
MERRA	Modern-Era Retrospective analysis for Research and Applications
MIPAS	Michelson Interferometer for Passive Atmospheric Sounding
MLS	Microwave Limb Sounder
MR	Meteorological Refresh mode
NASA	National Aeronautics and Space Administration
NAT	Nitric Acid Trihydrate
NDACC	Network for the Detection of Atmospheric Composition Change
NWP	Numerical Weather Prediction
PSC	Polar Stratospheric Cloud
QBO	Quasi-Biennial Oscillation
RMSE	Root Mean Square Error
SAD	Surface Area Densities
SLIMCAT	Single Layer Isentropic Model of Chemistry And Transport
SPARC	Stratosphere-troposphere Processes And their Role in Climate
SSA	Stratospheric Sulfate Aerosols
TOMS	Total Ozone Mapping Spectrometer
TUV	Tropospheric Ultraviolet and Visible model
UARS	Upper Atmosphere Research Satellite
UKMO	United Kingdom Meteorological Office

UV	Ultra-violet
VMR	Volume Mixing Ratio
WMO	World Meteorological Organization
3D-Var	Three-dimensional variational method
4D-Var	Four-dimensional variational method

Appendix A. List of Chemical Reactions

Table A1. Gas-phase reactions.

(*) $O + O_2 \rightarrow O_3$	(*) $O + O_3 \rightarrow 2\,O_2$	$O^{1D} + N_2 \rightarrow O + N_2$
$O^{1D} + N_2 \rightarrow N_2O$	$O^{1D} + O_2 \rightarrow O + O_2$	$O^{1D} + O_3 \rightarrow 2\,O_2$
$O^{1D} + O_3 \rightarrow O + O + O_2$	$O^{1D} + H_2O \rightarrow 2\,OH$	$O^{1D} + H_2 \rightarrow OH + H$
$O^{1D} + CH_4 \rightarrow CH_2O + H_2$	$O^{1D} + CH_4 \rightarrow CH_3 + OH$	$O^{1D} + N_2O \rightarrow O_2 + N_2$
$O^{1D} + N_2O \rightarrow NO + NO$	$O + O \rightarrow O_2$	$ClC_4 + O^{1D} \rightarrow 4\,Cl$
CFC11 $+ O^{1D} \rightarrow 3\,Cl + HF$	CFC12 $+ O^{1D} \rightarrow 2\,Cl + 2\,HF$	CFC113 $+ O^{1D} \rightarrow 3\,Cl + 3\,HF$
CFC114 $+ O^{1D} \rightarrow 2\,Cl + 4\,HF$	CFC115 $+ O^{1D} \rightarrow Cl + 5\,HF$	HCFC22 $+ O^{1D} \rightarrow Cl + 2\,HF$
HA1211 $+ O^{1D} \rightarrow Br + Cl + 2\,HF$	HA1301 $+ O^{1D} \rightarrow Br + 3\,HF$	$CH_3Br + O^{1D} \rightarrow Br$
HCFC22 $+ OH \rightarrow Cl + H_2O$	$CH_3Cl + OH \rightarrow HO_2 + Cl$	$CH_3Cl + Cl \rightarrow 2\,HCl$
$CH_3CCl_3 + OH \rightarrow 3\,Cl + H_2O$	$CH_3Br + OH \rightarrow Br + H_2O$	$CHBr_3 + OH \rightarrow 3\,Br + H_2O$
$H + O_2 \rightarrow HO_2$	$H + O_3 \rightarrow OH + O_2$	$H_2 + OH \rightarrow H_2O + H$
$OH + O_3 \rightarrow HO_2 + O_2$	$OH + O \rightarrow O_2 + H$	$OH + OH \rightarrow H_2O + O$
$OH + OH \rightarrow H_2O_2$	$HO_2 + O \rightarrow OH + O_2$	$HO_2 + O_3 \rightarrow OH + 2\,O_2$
$H + HO_2 \rightarrow 2\,OH$	$H + HO_2 \rightarrow H_2O + O$	$H + HO_2 \rightarrow H_2 + O_2$
$HO_2 + OH \rightarrow H_2O + O_2$	$HO_2 + HO_2 \rightarrow H_2O_2 + O_2$	$H_2O_2 + OH \rightarrow H_2O + HO_2$
$H_2O_2 + O \rightarrow OH + HO_2$	$H_2 + O \rightarrow OH + H$	$NO + O_3 \rightarrow NO_2 + O_2$
$NO + HO_2 \rightarrow NO_2 + OH$	$NO_2 + O \rightarrow NO + O_2$	$NO_2 + O \rightarrow NO_3 + O_2$
$NO + O \rightarrow NO_3 + O_2$	$NO_2 + O_3 \rightarrow NO_3 + O_2$	$NO_2 + OH \rightarrow HNO_3$
$NO_2 + HO_2 \rightarrow HNO_4$	$NO_3 + O \rightarrow O_2 + NO_2$	$NO_3 + NO \rightarrow 2\,NO_2$
$NO_3 + NO_2 \rightarrow N_2O_5$	$N_2O_5 \rightarrow NO_2 + NO_3$	$HNO_3 + OH \rightarrow H_2O + NO_3$
$HNO_4 + OH \rightarrow H_2O + NO_2 + O_2$	$HNO_4 \rightarrow HO_2 + NO_2$	$NO_3 + OH \rightarrow NO_2 + HO_2$
$NO_3 + HO_2 \rightarrow NO_2 + OH + O_2$	$NO_3 + HO_2 \rightarrow HNO_3 + O_2$	$N + NO \rightarrow N_2 + O$
$N + O_2 \rightarrow N_2 + O$	$NO + O \rightarrow NO_2 + O$	$Cl + O_2 \rightarrow ClOO$
$Cl + O_3 \rightarrow ClO + O_2$	$Cl + H_2 \rightarrow HCl + H$	$Cl + CH_4 \rightarrow HCl + CH_3$
$Cl + CH_2O \rightarrow HCl + HCO$	$Cl + HO_2 \rightarrow HCl + O_2$	$Cl + HO_2 \rightarrow OH + ClO$
$Cl + H_2O \rightarrow HCl + HO_2$	$Cl + HOCl \rightarrow Cl_2 + OH$	$Cl + HOCl \rightarrow ClO + HCl$
$Cl + OClO \rightarrow ClO + ClO$	$Cl + ClOO \rightarrow Cl_2 + O_2$	$Cl + ClOO \rightarrow ClO + ClO$
$ClO + O \rightarrow Cl + O_2$	$ClO + OH \rightarrow HO_2 + Cl$	$ClO + OH \rightarrow HCl + O_2$
$ClO + HO_2 \rightarrow O_2 + HOCl$	$ClO + NO \rightarrow NO_2 + Cl$	$ClO + NO_2 \rightarrow ClONO_2$
$ClO + ClO \rightarrow Cl + OClO$	$ClO + ClO \rightarrow Cl + ClOO$	$ClO + ClO \rightarrow Cl_2 + O_2$
$ClO + ClO \rightarrow Cl_2O_2$	$ClOO \rightarrow Cl + O_2$	$ClO + NO_3 \rightarrow ClOO + NO_2$
$Cl_2O_2 \rightarrow 2\,ClO$	$HCl + OH \rightarrow H_2O + Cl$	$HCl + O \rightarrow OH + Cl$
$OClO + O \rightarrow ClO + O_2$	$OClO + OH \rightarrow HOCl + O_2$	$OClO + NO \rightarrow ClO + NO_2$
$HOCl + O \rightarrow ClO + OH$	$HOCl + OH \rightarrow H_2O + ClO$	$Cl_2 + OH \rightarrow HOCl + Cl$
$ClONO_2 + O \rightarrow ClO + NO_3$	$ClONO_2 + OH \rightarrow HOCl + NO_3$	$ClONO_2 + Cl \rightarrow Cl_2 + NO_3$
$NO_2 + Cl \rightarrow ClNO_2$	$NO_3 + Cl \rightarrow ClO + NO_2$	$Cl_2 + O^{1D} \rightarrow ClO + Cl$
$HCl + O^{1D} \rightarrow OH + Cl$	$Cl_2O_2 + Cl \rightarrow Cl_2 + Cl + O_2$	$Br + O_3 \rightarrow BrO + O_2$
$Br + HO_2 \rightarrow HBr + O_2$	$Br + CH_2O \rightarrow HBr + HCO$	$Br + OClO \rightarrow BrO + ClO$
$BrO + O \rightarrow Br + O_2$	$BrO + HO_2 \rightarrow HOBr + O_2$	$BrO + NO \rightarrow Br + NO_2$
$BrO + NO_2 \rightarrow BrONO_2$	$BrO + ClO \rightarrow Br + OClO$	$BrO + ClO \rightarrow Br + ClOO$
$BrO + ClO \rightarrow BrCl + O_2$	$BrO + BrO \rightarrow 2\,Br + O_2$	$BrO + BrO \rightarrow Br_2 + O_2$
$HBr + OH \rightarrow Br + H_2O$	$HBr + O \rightarrow Br + OH$	$HOBr + O \rightarrow BrO + OH$
$Br_2 + OH \rightarrow HOBr + Br$	$BrO + OH \rightarrow HO_2 + Br$	$HBr + O^{1D} \rightarrow OH + Br$
$CO + OH \rightarrow H + CO_2$	$CH_4 + OH \rightarrow CH_3 + H_2O$	$CH_2O + OH \rightarrow HCO + H_2O$
$CH_2O + O \rightarrow HCO + OH$	$HCO + O_2 \rightarrow CO + HO_2$	$CH_3 + O_2 \rightarrow CH_3O_2$
$CH_3O + O_2 \rightarrow CH_2O + HO_2$	$CH_3O_2 + NO \rightarrow CH_3O + NO_2$	$CH_3O_2 + HO_2 \rightarrow CH_3OOH + O_2$
$CH_3O_2 + NO \rightarrow CH_3O + NO_2$	$CH_3O_2 + HO_2 \rightarrow CH_3OOH + O_2$	$CH_3OOH + OH \rightarrow CH_3O_2 + H_2O$
$CH_3OOH + OH \rightarrow CH_3O_2 + H_2O$	$CH_3OOH + OH \rightarrow CH_2O + HO_2 + OH$	$CH_2O + NO_3 \rightarrow CO + HO_2 + HNO_3$
$CO + O \rightarrow CO_2$		

Table A2. Heterogeneous reactions.

$ClONO_2 + H_2O \rightarrow HOCl + HNO_{3c}$	$ClONO_2 + HCl_c \rightarrow Cl_2 + HNO_{3c}$	$N_2O_5 + H_2O \rightarrow 2\,HNO_{3c}$
$N_2O_5 + HCl_c \rightarrow ClNO_2 + HNO_{3c}$	$HOCl + HCl \rightarrow Cl_2 + H_2O$	$BrONO_2 + H_2O \rightarrow HOBr + HNO_3$
$HOBr + HCl \rightarrow BrCl + H_2O$	$HOBr + HBr \rightarrow Br_2 + H_2O$	$BrONO_2 + HCl \rightarrow BrCl + HNO_3$

Table A3. Photolysis reactions.

(*) $O_2 + h\nu \rightarrow 2\,O$	(*) $O_3 + h\nu \rightarrow O + O_2$	$O_3 + h\nu \rightarrow O^{1D} + O_2$
$HO_2 + h\nu \rightarrow OH + O$	$H_2O_2 + h\nu \rightarrow 2\,OH$	$NO_2 + h\nu \rightarrow NO + O$
$NO_3 + h\nu \rightarrow NO_2 + O$	$NO_3 + h\nu \rightarrow NO + O_2$	$N_2O_5 + h\nu \rightarrow NO_2 + NO_3$
$HNO_3 + h\nu \rightarrow OH + NO_2$	$HNO_4 + h\nu \rightarrow OH + NO_3$	$HNO_4 + h\nu \rightarrow HO_2 + NO_2$
$Cl_2 + h\nu \rightarrow 2\,Cl$	$OClO + h\nu \rightarrow O + ClO$	$Cl_2O_2 + h\nu \rightarrow Cl + ClOO$
$HOCl + h\nu \rightarrow OH + Cl$	$ClONO_2 + h\nu \rightarrow Cl + NO_3$	$ClONO_2 + h\nu \rightarrow Cl + NO_2 + O$
$ClNO_2 + h\nu \rightarrow Cl + NO_2$	$BrCl + h\nu \rightarrow Br + Cl$	$BrO + h\nu \rightarrow Br + O$
$HOBr + h\nu \rightarrow Br + OH$	$BrONO_2 + h\nu \rightarrow Br + NO_3$	$BrONO_2 + h\nu \rightarrow BrO + NO_2$
$CH_2O + h\nu \rightarrow HCO + H$	$CH_2O + h\nu \rightarrow CO + H_2$	$CH_3OOH + h\nu \rightarrow CH_3O + OH$
$ClOO + h\nu \rightarrow O + ClO$		

Appendix B. Computation of the *J* Values

The rate of photodissociation is proportional to the in situ amount of the species i as

$$\frac{dc_i}{dt} = J_i c_i, \tag{A1}$$

where J_i whose units are s^{-1}, is the rate of photodissociation also called the J-values or the photodissociation frequency. This rate is determined by the number of photons available at a given altitude z and wavelength λ (the solar actinic flux $F(\lambda, z, \theta)$), the ability of the species (or molecule) to absorb these photons (the absorption cross-section $\sigma_i(\lambda)$) and the probability that the molecule will be photochemically destroyed following the absorption (the quantum yield $\phi_i(\lambda)$), integrated over all wavelengths

$$J_i = \int_\lambda \sigma_i(\lambda)\phi_i(\lambda)F(\lambda, z, \theta)d\lambda. \tag{A2}$$

The attenuation of the solar flux from the flux entering at the top of the atmosphere, $F(\lambda, \infty)$, occurs primarily from gas absorption due to O_2 and O_3 which can be computed from Beer–Lambert law

$$F(\lambda, z, \theta) = F(\lambda, \infty) \exp\left(-\left[\tau(O_2) + \tau(O_3)\right]\right), \tag{A3}$$

where τ's are the optical depths computed as

$$\tau(O_3) = \cos^{-1}\theta \int_z^\infty \sigma(O_3) c_{O_3}(z')dz' \tag{A4}$$

for O_3 and similarly for O_2. The above Equations (A3) and (A4) assume a plane-parallel atmosphere (valid for solar zenith angle $\theta < 75°$) and that scattering is negligible.

For most constituents, photolysis occurs mainly in the near-*UV* spectral region, which allows a further simplification of Equation (A2). In general, this expression needs to be integrated over a sufficiently small spectral interval to capture the wavelength dependency of the absorption cross-section. However, it is possible to capture the details while reducing the computational overhead using a J-table approach, where the computation is performed offline for all species in a multi-dimensional parameter space. In this study, we use the look-up tables of the photodissociation rates pre-computed by the TUV photolysis calculation package [118] using a pseudo-spectral two-stream discrete ordinate method for radiative transfer [119] for five typical ozone profiles. The model interpolates linearly the logarithm of the photodissociation rates in these tables as a function of geometric altitude, overhead column ozone and solar zenith angle.

Appendix C. Chemical Lower Boundary Conditions

Table A4. Chemical lower boundary conditions.

N_2O = 322 ppbv, CH_4 = 1.76 ppmv, CH_3Cl = 544 pptv, CH_3Br = 10.56 pptv
CFC-11 ($CFCl_3$) = 260 pptv, CFC-12 (CF_2Cl_2) = 544 pptv CFC-113 = 79.333 pptv, CFC-114 = 4.25 pptv, CFC-115 = 4.25 pptv
HA-1301 ($CBrF_3$) = 3.3 pptv, H-1211 ($CBrClF_2$) = 4.62 pptv, CCl_4 = 100 pptv
HCFC-22 ($CHClF_2$) = 170 pptv, CH_3CCl_3 = 45.333 pptv, $CHBr_3$ = 1.1733 pptv
O_3 = 20 ppbv, $O(^1D)$ = 1.E-21, $O(^3P)$ = 2.E-17
H = 2.E-22, OH = 1.E-15, HO_2 = 1 pptv, H_2O_2 = 2 ppbv, H_2 = 1.E-21
N = 1.E-21, NO = 1.E-13, NO_2 = 2 pptv, NO_3 = 3.E-14
ClOO = 1.E-21, OClO = 4.E-15, Cl = 9.E-19, ClO = 4.E-14 $ClNO_2$ = 1.E-21, HOCl = 2.E-13, Cl_2O_2 = 6.E-21, Cl_2 = 1.E-21
Br = 3.E-18, Br_2 = 1.E-21, BrO = 7.E-16, BrCl = 3.E-16, HOBr = 3.E-15
CH_3 = 1.E-21, CH_3O = 1.E-21, CH_3O_2 = 1.E-21, CH_2O = 1.E-21 CH_3OOH = 0.649 ppbv
HNO_3 = 2 pptv, HNO_4 = 3.E-14, N_2O_5 = 2.E-14, $ClONO_2$ = 1.E-13 $BrONO_2$ = 5.E-16
HBr = 4.E-15, HCl = 1 pptv, CO = 15 ppmv, HF = 1.E-21, HCO = 1.E-21 CO_2 = 380 ppmv

Appendix D. Mathematical Properties of CTM and MR Modes

In the MR mode, the meteorology, and in particular the wind field, is discontinuous before and after the meteorological analysis times t_A

$$\mathbf{V}(t_A^-) \neq \mathbf{V}(t_A^+). \tag{A5}$$

However, in offline CTM mode, the winds are time-continuous,

$$\mathbf{V}(t_A^-) = \mathbf{V}(t_A^+). \tag{A6}$$

Between analysis times, in both CTM and Meteorological Refresh modes, the evolution of the meteorology is time-continuous, and the chemical tracer field evolves as

$$\chi(t + \Delta t) = \chi(t) - \Delta t \mathbf{V}(t) \cdot \nabla \chi(t) \tag{A7}$$

for each time step Δt. In the time step preceding the analysis time we have

$$\chi(t_A^-) = \chi(t_A - \Delta t) - \Delta t \mathbf{V}(t_A - \Delta t) \cdot \nabla (t_A - \Delta t). \tag{A8}$$

Since there is no chemical analysis increment (as we consider here that there is no chemical assimilation), the chemical concentration field is continuous at t_A, i.e.,

$$\chi(t_A^-) = \chi(t_A^+), \tag{A9}$$

so that one time step after the analysis we have

$$\chi(t_A + \Delta t) = \chi(t_A^+) - \Delta t \mathbf{V}(t_A^+) \cdot \nabla (t_A^+). \tag{A10}$$

From Equation (A8) we have

$$\frac{d\chi}{dt}\Big|_{t_A^-} = \mathbf{V}(t_A^-) \cdot \nabla\chi(t_A), \tag{A11}$$

and from Equation (A10) we have

$$\frac{d\chi}{dt}\Big|_{t_A^+} = \mathbf{V}(t_A^+) \cdot \nabla\chi(t_A), \tag{A12}$$

and thus combining Equations (A11), (A12) we get in general

$$\frac{d\chi}{dt}\Big|_{t_A^+} - \frac{d\chi}{dt}\Big|_{t_A^-} = (\delta_A\mathbf{V}) \cdot \nabla\chi(t_A) \tag{A13}$$

where $\delta_A\mathbf{V} = \mathbf{V}(t_A^+) - \mathbf{V}(t_A^-)$ which is equal to zero for an offline CTM and is equal to the wind analysis increment in a coupled model run in MR mode. This result is summarized in Equation (18) in Section 4.

References

1. Ménard, R.; Gauthier, P.; Rochon, Y.; Robichaud, A.; de Grandpré, J.; Yang, Y.; Charrette, C.; Chabrillat, S. Coupled stratospheric chemistry-meteorology data assimilation. Part II: Weak and strong coupling. *Atmosphere* **2019**, *10*, 798. [CrossRef]
2. Lahoz, W.; Errera, Q. Constituent assimilation. In *Data Assimilation: Making Sense of Observations*; Lahoz, W., Khattatov, B., Ménard, R., Eds.; Springer: Berlin/Heidelberg, Germany, 2010; pp. 449–490. [CrossRef]
3. Brasseur, G.; Hauglustaine, D.; Walters, S.; Rasch, P.; Mfiller, J.; Granter, C.; Tie, X. MOZART, a global chemical transport model for ozone and related chemical tracers—1. Model description. *J. Geophys. Res.* **1998**, *103*, 28265–28289. [CrossRef]
4. Chipperfield, M.P. Multiannual simulations with a three-dimensional chemical transport model. *J. Geophys. Res.* **1999**, *104*, 1781–1805. [CrossRef]
5. Baklanov, A.; Brunner, D.; Carmichael, G.; Flemming, J.; Freitas, S.; Gauss, M.; Hov, O.; Mathur, R.; Schlünzen, K.H.; Seigneur, C.; et al. Key Issues for Seamless Integrated Chemistry–Meteorology Modeling. *Bull. Am. Meteorol. Soc.* **2017**, *98*, 2285–2292. [CrossRef] [PubMed]
6. Stouffer, R.J.; Eyring, V.; Meehl, G.A.; Bony, S.; Senior, C.; Stevens, B.; Taylor, K.E. CMIP5 Scientific Gaps and Recommendations for CMIP6. *Bull. Am. Meteorol. Soc.* **2017**, *98*, 95–105. [CrossRef]
7. Lamarque, J.F.; Emmons, L.; Hess, P.; Kinnison, D.; Tilmes, S.; Vitt, F.; Heald, C.; Holland, E.; Lauritzen, P.; Neu, J.; et al. CAM-chem: Description and evaluation of interactive atmospheric chemistry in the community earth system model. *Geosci. Model Dev.* **2012**, *5*, 369–411. [CrossRef]
8. Marsh, D.R.; Mills, M.J.; Kinnison, D.E.; Lamarque, J.F.; Calvo, N.; Polvani, L.M. Climate Change from 1850 to 2005 Simulated in CESM1(WACCM). *J. Clim.* **2013**, *26*, 7372–7391. [CrossRef]
9. Eyring, V.; Harris, N.; Rex, M.; Shepherd, T.; Fahey, D.; Amanatidis, G.; Austin, J.; Chipperfield, M.; Dameris, M.; Forster, P.F.; et al. A Strategy for Process-Oriented Validation of Coupled Chemistry–Climate Models. *Bull. Am. Meteorol. Soc.* **2005**, *86*, 1117–1134. [CrossRef]
10. *SPARC CCMVal Report on the Evaluation of Chemistry-Climate Models*; Technical Report; SPARC: Washington, DC, USA, 2010.
11. Zhang, Y. Online-coupled meteorology and chemistry models: History, current status, and outlook. *Atmos. Chem. Phys.* **2008**, *8*, 2895–2932. [CrossRef]
12. Baklanov, A.; Schlünzen, K.; Suppan, P.; Baldasano, J.; Brunner, D.; Aksoyoglu, S.; Carmichael, G.; Douros, J.; Flemming, J.; Forkel, R.; et al. Online coupled regional meteorology chemistry models in Europe: Current status and prospects. *Atmos. Chem. Phys.* **2014**, *14*, 317–398. [CrossRef]
13. Galmarini, S.; Hogrefe, C.; Brunner, D.; Baklanov, A.; Makar, P. Preface Article for the Atmospheric Environment Special Issue on AQMEII Phase 2. *Atmos. Environ.* **2015**, *115*, 340–344. [CrossRef]

14. Buchard, V.; Randles, C.; Da Silva, A.; Darmenov, A.; Colarco, P.; Govindaraju, R.; Ferrare, R.; Hair, J.; Beyersdorf, A.; Ziemba, L.; et al. The MERRA-2 Aerosol Reanalysis, 1980 Onward. Part II: Evaluation and Case Studies. *J. Clim.* **2017**, *30*, 6851–6872. [CrossRef]
15. Randles, C.A.; da Silva, A.M.; Buchard, V.; Colarco, P.R.; Darmenov, A.; Govindaraju, R.; Smirnov, A.; Holben, B.; Ferrare, R.; Hair, J.; et al. The MERRA-2 Aerosol Reanalysis, 1980 Onward. Part I: System Description and Data Assimilation Evaluation. *J. Clim.* **2017**, *30*, 6823–6850. [CrossRef]
16. Gaubert, B.; Arellano, A.F.J.; Barré, J.; Worden, H.M.; Emmons, L.K.; Tilmes, S.; Buchholz, R.; Vitt, F.; Raeder, K.; Collins, N.; et al. Toward a chemical reanalysis in a coupled chemistry-climate model: An evaluation of MOPITT CO assimilation and its impact on tropospheric composition. *J. Geophys. Res.* **2016**, *121*. [CrossRef]
17. Barré, J.; Gaubert, B.; Arellano, A.F.J.; Worden, H.M.; Edwards, D.P.; Deeter, M.N.; Anderson, J.L.; Raeder, K.; Collins, N.; Tilmes, S.; et al. Assessing the impacts of assimilating IASI and MOPITT CO retrievals using CESM-CAM-chem and DART. *J. Geophys. Res. Atmos.* **2015**, *120*, 10501–10529. [CrossRef]
18. Inness, A.; Baier, F.; Benedetti, A.; Bouarar, I.; Chabrillat, S.; Clark, H.; Clerbaux, C.; Coheur, P.; Engelen, R.J.; Errera, Q.; et al. The MACC reanalysis: An 8 yr data set of atmospheric composition. *Atmos. Chem. Phys.* **2013**, *13*, 4073–4109. [CrossRef]
19. WMO CCMM. *Coupled Chemistry-Meteorology/Climate Modelling (CCCM): Status and Relevance for Numerical Weather Prediction, Atmospheric Pollution and Climate Research*; Technical Report; WMO GAW: Geneva, Switzerland, 2016.
20. von Salzen, K.; Scinocca, J.F.; McFarlane, N.A.; Li, J.; Cole, J.N.S.; Plummer, D.; Verseghy, D.; Reader, M.C.; Ma, X.; Lazare, M.; et al. The Canadian Fourth Generation Atmospheric Global Climate Model (CanAM4). Part I: Representation of Physical Processes. *Atmosphere-Ocean* **2013**, *51*, 104–125. [CrossRef]
21. Kunz, A.; Pan, L.; Konopka, O.; Kinnison, D.; Tilmes, S. Chemical and dynamical discontinuity at extraropical tropopause based on START08 and WACCM analyses. *J. Geophys. Res.* **2011**, *116*. [CrossRef]
22. Froidevaux, L.; Kinnison, D.E.; Wang, R.; Anderson, J.; Fuller, R.A. Evaluation of CESM1 (WACCM) free-running and specified dynamics atmospheric composition simulations using global multispecies satellite data records. *Atmos. Chem. Phys.* **2019**, *19*, 4783–4821. [CrossRef]
23. de Grandpré, J.; Ménard, R.; Rochon, Y.J.; Charette, C.; Chabrillat, S.; Robichaud, A. Radiative Impact of Ozone on Temperature Predictability in a Coupled Chemistry–Dynamics Data Assimilation System. *Mon. Weather Rev.* **2009**, *137*, 679–692. [CrossRef]
24. Côté, J.; Gravel, S.; Methot, A.; Patoine, A.; Roch, M.; Staniforth, A. The operational CMC-MRB Global Environmental Multiscale (GEM) Model: Part I: Design considerations and formulation. *Mon. Weather Rev.* **1998**, *126*, 1373–1395. [CrossRef]
25. Errera, Q.; Fonteyn, D. Four-dimensional variational chemical assimilation of CRISTA stratospheric measurements. *J. Geophys. Res.* **2001**, *106*, 12,253–12,265. [CrossRef]
26. Errera, Q.; Daerden, F.; Chabrillat, S.; Lambert, J.C.; Lahoz, W.A.; Viscardy, S.; Bonjean, S.; Fonteyn, D. 4D-Var Assimilation of MIPAS chemical observations: Ozone and nitrogen dioxide analyses. *Atmos. Chem. Phys.* **2008**, *8*, 6169–6187. [CrossRef]
27. Skachko, S.; Errera, Q.; Ménard, R.; Christophe, Y.; Chabrillat, S. Comparison of the ensemble Kalman filter and 4D-Var assimilation methods using a stratospheric tracer transport model. *Geosci. Model Dev.* **2014**, *7*, 1451–1465. [CrossRef]
28. Skachko, S.; Ménard, R.; Errera, Q.; Christophe, Y.; Chabrillat, S. EnKF and 4D-Var data assimilation with chemical transport model BASCOE (version 05.06). *Geosci. Model Dev.* **2016**, *9*, 2893–2908. [CrossRef]
29. Chartrand, D.; de Grandpré, J.; McConnell, J.C. An introduction to stratospheric chemistry: Survey article. *Atmosphere-Ocean* **1999**, *37*, 309–367. [CrossRef]
30. London, J. Radiative energy sources and sinks in the stratosphere and mesosphere. In *Proceedings of the NATO Advanced Study Institute on Atmospheric Ozone*; Aiken, A., Ed.; Federal Aviation Administrator U.S. Department of Transportation: Washington, DC, USA, 1980; pp. 703–721.
31. Shepherd, T. The middle atmosphere. *J. Atmos. Sol.-Terr. Phys.* **2000**, *62*, 1587–1601. [CrossRef]
32. Shepherd, T. Issues in Stratosphere-troposphere Coupling. *J. Meteorol. Soc. Japan. Ser. II* **2002**, *80*, 769–792. [CrossRef]
33. Warn, T.; Warn, H. The Evolution of a Nonlinear Critical Level. *Stud. Appl. Math.* **1978**, *59*, 37–71. [CrossRef]
34. McIntyre, M.; Palmer, T. Breaking planetary waves in the stratosphere. *Nature* **1983**, *305*, 593–600. [CrossRef]

35. Waugh, D.; Plumb, R.; Atkinson, R.; Schoeberl, M.; Lait, L.; Newman, P.; Loewenstein, M.; Toohey, D.; Avallone, L.; Webster, C.; et al. Transport of material out of the stratospheric Arctic vortex by Rossby wave breaking. *J. Geophys. Res.* **1994**, *99*, 1071–1088. [CrossRef]
36. Homeyer, C.R.; Bowman, K.P. Rossby Wave Breaking and Transport between the Tropics and Extratropics above the Subtropical Jet. *J. Atmos. Sci.* **2013**, *70*, 607–626. [CrossRef]
37. Ménard, R.; Chang, L.P. Assimilation of Stratospheric Chemical Tracer Observations Using a Kalman Filter. Part II: χ^2-Validated Results and Analysis of Variance and Correlation Dynamics. *Mon. Weather Rev.* **2000**, *128*, 2672–2686. [CrossRef]
38. McLandress, C.; McFarlane, N. Interactions between Orographic Gravity Wave Drag and Forced Stationary Planetary Waves in the Winter Northern Hemisphere Middle Atmosphere. *J. Atmos. Sci.* **1993**, *50*, 1966–1990. [CrossRef]
39. Hines, C. Doppler-spread parameterization of gravity-wave momentum deposition in the middle atmosphere. Part 1: Basic formulation. *J. Atmos. Sol.-Terr. Phys.* **1997**, *59*, 371–386. [CrossRef]
40. Hines, C. Doppler-spread parameterization of gravity-wave momentum deposition in the middle atmosphere. Part 2: Broad and quasi monochromatic spectra, and implementation. *J. Atmos. Sol.-Terr. Phys.* **1997**, *59*, 387–400. [CrossRef]
41. Brewer, A.W. Evidence for a world circulation provided by the measurements of helium and water vapour distribution in the stratosphere. *Q. J. R. Meteorol. Soc.* **1949**, *75*, 351–363. [CrossRef]
42. Dobson, G.; Massey, H. Origin and distribution of the polyatomic molecules in the atmosphere. *Proc. R. Soc. Lond. Ser. A* **1956**, *236*, 187–193. [CrossRef]
43. Froidevaux, L.; Allen, M.; Berman, S.; Daughton, A. The mean ozone profile and its temperature sensitivity in the upper stratosphere and lower mesosphere: An analysis of LIMS observations. *J. Geophys. Res.* **1989**, *94*, 6389–6417. [CrossRef]
44. Ward, W.; Oberheide, J.; Reise, M.; Preusse, P.; Offerman, D. Planetary wave two signatures in CHRISTA 2 ozone and temperature data. In *Atmospheric Science across the Stratopause*; Geophysical Monograph Series (Book 123); Siskind, D.E., Eckermann, S.D., Summers, M.E., Eds.; AGU Press: Washington, DC, USA, 2000; pp. 319–326.
45. Barnett, J.J.; Houghton, J.T.; Pyle, J.A. The temperature dependence of the ozone concentration near the stratopause. *Q. J. R. Meteorol. Soc.* **1975**, *101*, 245–257. [CrossRef]
46. Haigh, J.; Pyle, J. Ozone perturbation experiments in a two-dimensional circulation model. *Q. J. R. Meteorol. Soc.* **1982**, *108*, 551–574. [CrossRef]
47. Smith, A. Numerical simulation of global variations of temperature, ozone, and trace species in the stratosphere. *J. Geophys. Res.* **1995**, *100*, 1253–1269. [CrossRef]
48. Kiehl, J.; Solomon, S. On the Radiative Balance of the Stratosphere. *J. Atmos. Sci.* **1986**, *43*, 1525–1534. [CrossRef]
49. McLinden, C.; Olsen, S.; Hannegan, B.; Wild, O.; Prather, M.; Sundet, J. Stratospheric ozone in 3-D models: A simple chemistry and the cross-tropopause flux. *J. Geophys. Res.* **2000**, *105*, 14653–14665. [CrossRef]
50. Oberheide, J.; Lehmacher, G.A.; Offermann, D.; Grossmann, K.U.; Manson, A.H.; Meek, C.E.; Schmidlin, F.J.; Singer, W.; Hoffmann, P.; Vincent, R.A. Geostrophic wind fields in the stratosphere and mesosphere from satellite data. *J. Geophys. Res. Atmos.* **2002**, *107*, CRI 3-1–CRI 3-18. [CrossRef]
51. De Grandpré, J.; Beagley, S.R.; Fomichev, V.I.; Griffioen, E.; McConnell, J.C.; Medvedev, A.S.; Shepherd, T.G. Ozone climatology using interactive chemistry: Results from the Canadian Middle Atmosphere Model. *J. Geophys. Res.* **2000**, *105*, 26475–26491. [CrossRef]
52. Morcrette, J.J. *Ozone-Radiation Interactions in the ECMWF Forecast System*; Technical Report 375; European Center for Medium-Range Weather Forecasting: Reading, UK, 2013.
53. Plumb, R.; Ko, M. Interrelationships between mixing ratios of long-lived stratospheric constituents. *J. Geophys. Res.* **1992**, *97*, 10145–10156. [CrossRef]
54. Holton, J. A dynamically based transport parameterization for one-dimensional photochemical models of the stratosphere. *J. Geophys. Res.* **1986**, *91*, 2681–2686. [CrossRef]
55. Gauthier, P.; Charette, C.; Fillion, L.; Koclas, P.; Laroche, S. Implementation of a 3D variational data assimilation system at the Canadian Meteorological Centre. Part I: The global analysis. *Atmosphere-Ocean* **1999**, *37*, 103–156. [CrossRef]

56. Gauthier, P.; Tanguay, M.; Laroche, S.; Pellerin, S.; Morneau, J. Extension of the 3DVAR to 4DVAR: Implementation of 4DVAR at the Meteorological Service of Canada. *Mon. Weather Rev.* **2007**, *135*, 2339–2354. [CrossRef]
57. Charron, M.; Polavarapu, S.; Buehner, M.; Vaillancourt, P.A.; Charette, C.; Roch, M.; Morneau, J.; Garand, L.; Aparicio, J.; MacPherson, S.; et al. The Stratospheric Extension of the Canadian Global Deterministic Medium-Range Weather Forecasting System and Its Impact on Tropospheric Forecasts. *Mon. Weather Rev.* **2012**, *140*, 1924–1944. [CrossRef]
58. Lin, S.J.; Rood, R. Multidimensional Flux-Form Semi-Lagrangian Transport Schemes. *Mon. Weather Rev.* **1996**, *124*, 2046–2070. [CrossRef]
59. Côté, J.; M., R.; Staniforth, A.; Fillion, L. A variable resolution semi-Lagrangian finite-element global model of the shallow water equations. *Mon. Weather Rev.* **1993**, *121*, 231–243. [CrossRef]
60. Li, J.; Barker, H. A Radiation Algorithm with Correlated- Distribution. Part I: Local Thermal Equilibrium. *J. Atmos. Sci.* **2005**, *62*, 286–309. [CrossRef]
61. Fortuin, F.P.J.; Kelder, H. An ozone climatology based on ozonesonde and satellite measurements. *J. Geophys. Res.* **1998**, *103*, 31709–31734. [CrossRef]
62. Feist, D.G.; Geer, A.J.; Müller, S.; Kämpfer, N. Middle atmosphere water vapour and dynamical features in aircraft measurements and ECMWF analyses. *Atmos. Chem. Phys.* **2007**, *7*, 5291–5307. [CrossRef]
63. Brasseur, G.; Solomon, S. *Aeronomy of the Middle Atmosphere*; Reidel: Norwell, MA, USA, 1984.
64. Sander, S.; Friedl, R.; Golden, D.; Kurylo, M.; Huie, R.; Orkin, V.; Moortgaat, G.; Ravishankara, A.; Kolb, C.; Molina, M. *Chemical Kinetics and Photochemical Data for Use in Atmospheric Studies*; Technical Report Publication 00-3; JPL, Jet Propulsion Laboratory: Pasadena, CA, USA, 2003.
65. Lowe, D.; MacKenzie, A.R. Polar stratospheric cloud microphysics and chemistry. *J. Atmos. Sol.-Terr. Phys.* **2008**, *70*, 13–40. [CrossRef]
66. Errera, Q. Assimilation des Observations Chimiques StratosphéRiques CRISTA Suivant La MéThode Variationelle à Quatre Dimensions. Ph.D. Thesis, Université Libre de Bruxelles, Bruxelles, Belgique, 2002.
67. Yudin, V.; Khattatov, B. Introduction to atmospheric chemistry and constituent transport. In *Data Assimilation*; Lahoz, W., Khattatov, B., Ménard, R., Eds.; Springer: Berlin/Heidelberg, Germany, 2010; pp. 409–430.
68. Hairer, E.; Wanner, G. *Solving Ordinary Differential Equations II*; Springer: Berlin/Heidelberg, Germany, 1996.
69. Press, W.H.; Teukolsky, S.A.; Vetterling, W.T.; Flannery, B.P. *Numerical Recipes in FORTRAN: The Art of Scientific Computing*, 2nd ed.; Cambridge University Press: New York, NY, USA, 1992.
70. Sportisse, B. A review of current issues in air pollution modeling and simulation. *Comput. Geosci.* **2007**, *11*, 159–181. [CrossRef]
71. Sandu, A.; Verwer, J.; Blom, J.; Spee, E.; Carmichael, G.; Potra, F. Benchmarking stiff ode solvers for atmospheric chemistry problems II, Rosenbrock solvers. *Atmos. Environ.* **1997**, *31*, 3459–3472. [CrossRef]
72. Damian, V.; Sandu, A.; Damian, M.; Potra, F.; Carmicheal, G. The Kinetic PreProcessor KPP—A software environment for solving chemical kinetics. *Comput. Chem. Eng.* **2002**, *26*, 1567–1579. [CrossRef]
73. Beljaards, A.; Bechtold, P.; Khöler, M.; Morcrette, J.J.; Tompkins, A.; Viterbo, P.; Wedi, N. *Numerical Schemes for Parametrization*; Technical Report; ECMWF: Reading, UK, 1991.
74. Beljaars, A.; Balsamo, G.; Bechtold, P.; Bozzo, A.; Forbes, R.; Hogan, R.J.; Köhler, M.; Morcrette, J.J.; Tompkins, A.M.; Viterbo, P.; et al. The Numerics of Physical Parametrization in the ECMWF Model. *Front. Earth Sci.* **2018**, *6*, 137. [CrossRef]
75. Caya, A.; Laprise, R.; Zwack, P. Consequences of Using the Splitting Method for Implementing Physical Forcings in a Semi-Implicit Semi-Lagrangian Model. *Mon. Wea. Rev.* **1998**, *126*, 1707–1713. [CrossRef]
76. Williamson, D. Time-Split versus Process-Split Coupling of Parameterizations and Dynamical Core. *Mon. Weather Rev.* **2002**, *130*, 2024–2041. [CrossRef]
77. Weaver, C.; Douglass, A.; Rood, R. Thermodynamic balance of three-dimensional stratospheric winds derived from data assimilation procedure. *J. Atmos. Sci.* **1993**, *50*, 2987–2993. [CrossRef]
78. Chipperfield, M. New version of the TOMCAT/SLIMCAT off-line chemical transport model: Intercomparison of stratospheric tracer experiments. *Q. J. R. Meteorol. Soc.* **2006**, *132*, 1179–1203. [CrossRef]
79. Garand, L.; Deblonde, G.; Anselmo, D.; Aparicio, J.; Beaulne, A.; Hallé, J.; MacPherson, S.; Wagner, N. *Experience with Bias Correction at CMC*; Proceedings of the ECMWF/EUMETSAT NWP-SAF Workshop on Bias Estimation and Correction in Data Assimilation; ECMWF: Reading, UK, 2005, pp. 153–162.

80. Ménard, R. Bias estimation. In *Data Assimilation: Making Sense of Observations*; Lahoz, W., Khattatov, B., Ménard, R., Eds.; Springer: Berlin/Heidelberg, Germany, 2010; pp. 113–135. [CrossRef]
81. Tanguay, M.; Bartello, P.; Gauthier, P. Four-dimensional data assimilation with a wide range of scales. *Tellus* **1995**, *47A*, 974–997. [CrossRef]
82. Laroche, S.; Gauthier, P. A validation of the incremental formulation of 4D variational data assimilation in a nonlinear barotropic flow. *Tellus* **1998**, *50A*, 557–572. [CrossRef]
83. Koshyk, J.N.; Boville, B.A.; Hamilton, K.; Manzini, E.; Shibata, K. Kinetic energy spectrum of horizontal motions in middle-atmosphere models. *J. Geophys. Res.* **1999**, *104*, 27177–27190. [CrossRef]
84. Batello, P. Using low-resolution winds to deduce fine structure in tracers. *Atmosphere-Ocean* **2000**, *38*, 303–320. [CrossRef]
85. Haynes, P.; Vanneste, J. Stratospheric tracer spectra. *J. Atmos. Sci.* **2004**, *61*, 161–178. [CrossRef]
86. Bacmeister, J.; Eckermann, S.; Newman, P.; Lait, L.; Chan, K.; Loewenstein, M.; Proffitt, M.; Gary, B. Stratospheric horizontal wavenumber spectra of winds, potential temperature and tracers observed by high-altitude aircraft. *J. Geosphys. Res.* **1996**, *101*, 9441–9470. [CrossRef]
87. Gage, K.S.; Nastrom, G.D. Theoretical Interpretation of Atmospheric Wavenumber Spectra of Wind and Temperature Observed by Commercial Aircraft During GASP. *J. Atmos. Sci.* **1986**, *43*, 729–740. [CrossRef]
88. Waugh, D.; Plumb, R. Contour advection with surgery: A technique for investigating finescale structure in tracer transport. *J. Atmos. Sci.* **1994**, *51*, 530–540. [CrossRef]
89. Strahan, S.E.; Polansky, B.C. Meteorological implementation issues in chemistry and transport models. *Atmos. Chem. Phys.* **2006**, *6*, 2895–2910. [CrossRef]
90. Sinnhuber, B.M.; Stiller, G.; Ruhnke, R.; von Clarmann, T.; Kellmann, S.; Aschmann, J. Arctic winter 2010/2011 at the brink of an ozone hole. *Geophys. Res. Lett.* **2011**, *38*. [CrossRef]
91. Kirner, O.; Müller, R.; Ruhnke, R.; Fischer, H. Contribution of liquid, NAT and ice particles to chlorine activation and ozone depletion in Antarctic winter and spring. *Atmos. Chem. Phys.* **2015**, *15*, 2019–2030. [CrossRef]
92. Errera, Q.; Ménard, R. Technical Note: Spectral representation of spatial correlations in variational assimilation with grid point models and application to the Belgian Assimilation System for Chemical Observations (BASCOE). *Atmos. Chem. Phys.* **2012**, *12*, 10015–10031. [CrossRef]
93. Louet, J. The Envisat Mission and System. 2001. Available online: http://www.esa.int/esapub/bulletin/bullet106/bul106_1.pdf (accessed on 18 October 2019).
94. Envisat Science Team. Validation Workshop Proceedings. 2002. Available online: https://envisat.esa.int/pub/ESA_DOC/envisat_val_1202/proceedings/ (accessed on 18 October 2019).
95. MIPAS Science Team. MIPAS Geophysical Validation (Special Issue). *Atmos. Chem. Phys.* **2009**. Available online: //envisat.esa.int/pub/ESA_DOC/envisat_val_1202/proceedings/ (accessed on 18 October 2019).
96. Ridolfi, M.; Blum, U.; Carli, B.; Catoire, V.; Ceccherini, S.; Claude, H.; De Clercq, C.; Fricke, K.H.; Friedl-Vallon, F.; Iarlori, M.; et al. Geophysical validation of temperature retrieved by the ESA processor from MIPAS/ENVISAT atmospheric limb-emission measurements. *Atmos. Chem. Phys.* **2007**, *7*, 4459–4487. [CrossRef]
97. Cortesi, U.; Lambert, J.C.; De Clercq, C.; Bianchini, G.; Blumenstock, T.; Bracher, A.; Castelli, E.; Catoire, V.; Chance, K.V.; De Mazière, M.; et al. Geophysical validation of MIPAS-ENVISAT operational ozone data. *Atmos. Chem. Phys.* **2007**, *7*, 4807–4867. [CrossRef]
98. Pappalardo, G.; Colavitto, T.; Congeduti, F.; Cuomo, V.; Deuber, B.; Kämpfer, N.; Iarlori, M.; Lucia, M.; Rizi, V. *Validation of MIPAS Water Vapor Products by Ground Based Measurements*; European Space Agency, (Special Publication) ESA SP: Paris, France, 2004.
99. Raspollini, P.; Belotti, C.; Burgess, A.; Carli, B.; Carlotti, M.; Ceccherini, S.; Dinelli, B.M.; Dudhia, A.; Flaud, J.M.; Funke, B.; et al. MIPAS level 2 operational analysis. *Atmos. Chem. Phys.* **2006**, *6*, 5605–5630. [CrossRef]
100. Wang, D.Y.; Höpfner, M.; Blom, C.E.; Ward, W.E.; Fischer, H.; Blumenstock, T.; Hase, F.; Keim, C.; Liu, G.Y.; Mikuteit, S.; et al. Validation of MIPAS HNO_3 operational data. *Atmos. Chem. Phys.* **2007**, *7*, 4905–4934. [CrossRef]
101. Wetzel, G.; Bracher, A.; Funke, B.; Goutail, F.; Hendrick, F.; Lambert, J.C.; Mikuteit, S.; Piccolo, C.; Pirre, M.; Bazureau, A.; et al. Validation of MIPAS-ENVISAT NO_2 operational data. *Atmos. Chem. Phys.* **2007**, *7*, 3261–3284. [CrossRef]

102. Reber, C.A.; Trevathan, C.E.; McNeal, R.J.; Luther, M.R. The Upper Atmosphere Research Satellite (UARS) mission. *J. Geophys. Res. Atmos.* **1993**, *98*, 10643–10647. [CrossRef]
103. UARS Science Team; Rood, R.B.; Geller, M.A. (Eds.) UARS Data and Scientific Results (Special Issue). *J. Atmos. Sci.* **1994**, *51*, 2781–3105.
104. UARS Science Team; Gille, J.C.; Massie, S.T.; Mankin, W.G. (Eds.) Evaluation of the UARS Data (Special Issue). *J. Geophys. Res. Atmos.* **1996**, *D6*, 9539–10473. [CrossRef]
105. Russell, J.M., III; Gordley, L.L.; Park, J.H.; Drayson, S.R.; Hesketh, W.D.; Cicerone, R.J.; Tuck, A.F.; Frederick, J.E.; Harries, J.E.; Crutzen, P.J. The Halogen Occultation Experiment. *J. Geophys. Res. Atmos.* **1993**, *98*, 10777–10797. [CrossRef]
106. Morris, G.A.; Gleason, J.F.; Russell, J.M., III; Schoeberl, M.R.; McCormick, M.P. A comparison of HALOE V19 with SAGE II V6.00 ozone observations using trajectory mapping. *J. Geophys. Res. Atmos.* **2002**, *107*, ACH 10-1–ACH 10-9. [CrossRef]
107. Harries, J.E.; Russell, J.M., III; Tuck, A.F.; Gordley, L.L.; Purcell, P.; Stone, K.; Bevilacqua, R.M.; Gunson, M.; Nedoluha, G.; Traub, W.A. Validation of measurements of water vapor from the Halogen Occultation Experiment (HALOE). *J. Geophys. Res. Atmos.* **1996**, *101*, 10205–10216. [CrossRef]
108. Park, J.H.; Russell, J.M., III; Gordley, L.L.; Drayson, S.R.; Benner, D.C.; McInerney, J.M.; Gunson, M.R.; Toon, G.C.; Sen, B.; Blavier, J.F.; et al. Validation of Halogen Occultation Experiment CH4 measurements from the UARS. *J. Geophys. Res. Atmos.* **1996**, *101*, 10183–10203. [CrossRef]
109. Lindenmaier, R.; Strong, K.; Batchelor, R.L.; Bernath, P.F.; Chabrillat, S.; Chipperfield, M.P.; Daffer, W.H.; Drummond, J.R.; Feng, W.; Jonsson, A.I.; et al. A study of the Arctic NOy budget above Eureka, Canada. *J. Geophys. Res. Atmos.* **2011**, *116*. [CrossRef]
110. GEM-BACH IPY Data Set. Available online: https://www.sparc-climate.org/data-centre/data-access/sparc-ipy/ (accessed on 20 October 2014).
111. Batchelor, R.L.; Strong, K.; Lindenmaier, R.; Mittermeier, R.L.; Fast, H.; Drummond, J.R.; Fogal, P.F. A New Bruker IFS 125HR FTIR Spectrometer for the Polar Environment Atmospheric Research Laboratory at Eureka, Nunavut, Canada: Measurements and Comparison with the Existing Bomem DA8 Spectrometer. *J. Atmos. Ocean. Technol.* **2009**, *26*, 1328–1340. [CrossRef]
112. Batchelor, R.L.; Kolonjari, F.; Lindenmaier, R.; Mittermeier, R.L.; Daffer, W.; Fast, H.; Manney, G.; Strong, K.; Walker, K.A. Four Fourier transform spectrometers and the Arctic polar vortex: instrument intercomparison and ACE-FTS validation at Eureka during the IPY springs of 2007 and 2008. *Atmos. Meas. Tech.* **2010**, *3*, 51–66. [CrossRef]
113. Rodgers, C.D.; Connor, B.J. Intercomparison of remote sounding instruments. *J. Geophys. Res. Atmos.* **2003**, *108*. [CrossRef]
114. Rösevall, J.D.; Murtagh, D.P.; Urban, J. Ozone depletion in the 2006/2007 Arctic winter. *Geophys. Res. Lett.* **2007**, *34*. [CrossRef]
115. Sagi, K.; Murtagh, D. A long term study of polar ozone loss derived from data assimilation of Odin/SMR observations. *Atmos. Chem. Phys. Discuss.* **2016**, *2016*, 1–27. [CrossRef]
116. Ostler, A.; Sussmann, R.; Patra, P.K.; Houweling, S.; De Bruine, M.; Stiller, G.P.; Haenel, F.J.; Plieninger, J.; Bousquet, P.; Yin, Y.; et al. Evaluation of column-averaged methane in models and TCCON with a focus on the stratosphere. *Atmos. Meas. Tech.* **2016**, *9*, 4843–4859. [CrossRef]
117. Wang, Z.; Warneke, T.; Deutscher, N.M.; Notholt, J.; Karstens, U.; Saunois, M.; Schneider, M.; Sussmann, R.; Sembhi, H.; Griffith, D.W.T.; et al. Contributions of the troposphere and stratosphere to CH_4 model biases. *Atmos. Chem. Phys.* **2017**, *17*, 13283–13295. [CrossRef]
118. Madronich, S.; Flocke, S. The role of solar radiation in atmospheric chemistry. In *Handbook of Environmental Chemistry*; Boule, P., Ed.; Springer: Heidelberg, Germany, 1998; pp. 1–26.
119. Toon, O.; McKay, C.; Ackerman, T.; Santhanam, K. Rapid calculation of radiative heating rates and photodissociation rates in inhomogeneous multiple scattering atmospheres. *J. Geophys. Res.* **1989**, *94*, 16287–16301. [CrossRef]